

Downslope Windstorms of San Diego County. Part I: A Case Study

YANG CAO AND ROBERT G. FOVELL

Department of Atmospheric and Oceanic Sciences, University of California, Los Angeles, Los Angeles, California

(Manuscript received 9 April 2015, in final form 27 October 2015)

ABSTRACT

The “Santa Ana” wind is an offshore flow that affects Southern California periodically during the winter half of the year, typically between September and May. The winds can be locally gusty, particularly in the complex terrain of San Diego County, where the winds have characteristics of downslope windstorms. These winds can cause and/or rapidly spread wildfires, the threat of which is particularly acute during the autumn season before the onset of winter rains. San Diego’s largest fires, including the Cedar fire of 2003 and Witch Creek fire of 2007, occurred during Santa Ana wind events.

A case study of downslope flow during a moderately intense Santa Ana event during mid-February 2013 is presented. Motivated by the need to forecast winds impinging on electrical lines, the authors make use of an exceptionally dense network of near-surface observations in San Diego County to calibrate and verify simulations made utilizing the Advanced Research version of the Weather Research and Forecasting (WRF) Model, which in turn is employed to augment the observations. Results demonstrate that this particular Santa Ana episode consists of two pulses separated by a protracted lull. During the first pulse, the downslope flow is characterized by a prominent hydraulic jumplike feature, while during the second one the flow possesses a clear temporal progression of winds downslope. WRF has skill in capturing the evolution and magnitude of the event at most locations, although most model configurations overpredict the observed sustained wind and the forecast bias is itself biased.

1. Introduction

Southern California is known for its “Santa Ana” winds, which were named after a city and canyon in Orange County, California. The Santa Anas are very dry, sometimes hot, offshore winds directed from the Great Basin and Mojave Desert over the mountains and through the passes of Southern California (cf. [Sommers 1978](#); [Small 1995](#)) that can produce gusts exceeding 45 m s^{-1} (100 mph) in favored areas.¹ The winds evince terrain-associated amplification of the mountain gap and

downslope varieties ([Huang et al. 2009](#); [Hughes and Hall 2010](#)). Santa Ana events occur most frequently between October and February, with December being the peak month ([Raphael 2003](#); [Jones et al. 2010](#)). Its season is often thought of as extending from September to April, although recent years (2013 and 2014) have seen events of significant strength during the month of May.

Although the Santa Anas tend to form most frequently in midwinter, the most dangerous events often occur in autumn, before the winter rains have begun ([Sommers 1978](#); [Westerling et al. 2004](#)). At that time, the vegetation tends to be extremely dry, and fire danger is elevated owing to the combination of low to very low humidity and strong winds that can spark and spread flames. Autumn fires historically have the potential to be very large in area, being fanned by the Santa Ana winds ([Chang and Schoenberg 2011](#)).

Santa Ana events result when cooler air spills across the Great Basin, becoming partially dammed by the mountains that separate Southern California from the inland deserts. This increases the horizontal gradient in sea level pressure (SLP) and helps to enhance flow speeds through prominent terrain gaps such as the Cajon Pass (leading to

¹Examples: On 21 October 2007, the weather station on Laguna Peak, overlooking Pt. Mugu, recorded a 50 m s^{-1} (111.5 mph) wind gust. More recently, on 30 April 2014, a station in San Diego County (Sill Hill, SILSD) reported a 45 m s^{-1} (101 mph) gust, and remained above 40 m s^{-1} (90 mph) for a total of five nonconsecutive hours.

Corresponding author address: Robert Fovell, Atmospheric and Oceanic Sciences, University of California, Los Angeles, 405 Hilgard Ave., Los Angeles, CA 90095.
E-mail: rfovell@ucla.edu

Santa Ana) and through the Soledad Pass (northwest of Los Angeles), creating prominent wind corridors in the northern part of the Los Angeles basin (Jackson et al. 2013). Wind speeds can also be very large in San Diego County, where the terrain gaps appear less prominent but mountain heights are also generally lower. The flow across this topography shares many characteristics of classic downslope windstorms (e.g., Huang et al. 2009).

Downslope windstorms are a type of large-amplitude mountain wave that can produce strong, often gusty winds on the lee side of a mountain barrier (Durran 1990, 2003; Jackson et al. 2013). They are observed in many areas of the world, and carry such names as the bora, chinook, foehn, zonda and taku winds (e.g., Schamp 1964; Durran 2003). Windstorms require a sufficiently large mountain barrier, and a terrain-dependent magnitude of cross-barrier winds, along with another ingredient such as an elevated inversion (e.g., Vosper 2004; Sheridan and Vosper 2006), Scorer parameter layering (e.g., Durran 1986), or a critical level either associated with the mean state (e.g., Durran and Klemp 1987) or generated by wave breaking (e.g., Peltier and Clark 1979). Subsidence associated with downslope windstorms can cause very low relative humidities near the surface, particularly if the air mass starts with low absolute humidity.

In complex terrain, the wind can vary greatly over small distances and gustiness is common in downslope windstorms, which may include rotors and subrotors embedded in the flow (Doyle and Durran 2004; Jackson et al. 2013). Terrain-amplified winds and gusts can knock down trees and power lines, starting and spreading fires, making accurate forecasts in this region extremely important. Proper model verification, however, can be hampered by the sparseness of the surface network, the absence of stations in wind-prone areas, as well as deficiencies in anemometer placement. As an example, on 21 October 2007, the Witch Creek fire was sparked by wind-whipped power lines located about 20 m above ground level (AGL), and was driven by an especially strong Santa Ana winds to become one of the largest fires in California history.² It is nearly certain that the meteorological stations that existed at the time did not fully capture the ferocity of the winds experienced at the initiation site of that or other fires that started during this windstorm.

Despite steady improvement in operational numerical weather prediction models over the last several decades as well as advancements in the understanding of mountain meteorology dynamics, forecast skill for downslope windstorms is still limited by several factors, including dependence and/or sensitivity to model resolution (e.g., Reinecke and Durran 2009b; Jackson et al. 2013), numerical schemes (e.g., Reinecke and Durran 2009b), vertical coordinates and diffusion (e.g., Smith et al. 2007), physical formulations [especially the boundary layer; see Smith (2007)] and initial condition uncertainties (e.g., Reinecke and Durran 2009a). Our work was motivated by the need to forecast winds that could affect electrical transmission lines in San Diego County operated by the San Diego Gas and Electric (SDG&E) company. Operational products were viewed by the meteorologists tasked with anticipating wind threats in the electric network as insufficiently skillful (B. D'Agostino and S. Vanderburg 2012, personal communication). In particular, even available high-resolution (4-km horizontal grid spacing or better) products permitted the strong near-surface winds to extend downslope too far and too often, resulting in false alarms and a waste of resources.

In this part, we examine the skill of the Advanced Research version of the Weather Research and Forecasting (WRF) Model (Skamarock et al. 2008) core in forecasting Santa Ana winds in San Diego County. High spatial resolution is focused over this area, especially over the area's roughly north-south mountain range that serves to amplify the winds. Model forecasts are verified against wind observations reported by the SDG&E mesonet, a recently installed and exceptionally dense surface observing network of (presently) more than 140 stations sited primarily in well-exposed, wind-prone areas on the west-facing slopes of the county's mountains. Numerous combinations of model physical parameterizations were examined, for this and similar events, to identify the configuration that best captures the magnitude, temporal evolution, and spatial extent of the winds. Although the verification observations are still confined near the surface, we will show that the SDG&E network helps reveal model weaknesses and suggest remedies that might not have been detectable from a less-extensive set of observations.

The structure of this paper is as follows. The available observations, model experimental design, and verification strategy are presented in section 2. The mid-February 2013 event is described via SDG&E network observations in section 3. Section 4 presents the model simulations and comparisons with the observations, and the summary composes the final section.

² According to information obtained from the California Department of Forestry and Fire Protection (Cal Fire), the Witch Creek fire was the third largest California wildfire since 1932 upon its containment, and is ranked sixth largest as of this writing.

2. Data and methods

a. Available observations

Observations are crucial for vetting a numerical model, but there are several significant challenges involved. First of all, most of the data available for verification are located very close to the surface, and even these have historically been relatively sparse. With respect to airflow, the relevant information comes in the form of “sustained winds,” which are temporally averaged quantities composed of discrete samples measured by anemometers. While the [WMO \(2010\)](#) provides some guidelines for sustained wind collection at synoptic stations (specifying a 10-m anemometer mounting height above local open ground and removed from obstacles, and a 10-min averaging period), it remains that networks tend to differ with respect to sensor hardware, mounting height, station siting guidelines and sampling, and averaging and reporting intervals. All of these can dramatically impact the magnitudes of winds and gusts that are reported, complicating the verification process.

As an example, most (not all) ASOS stations report sustained winds at 10 m AGL, but averaged over a 2-min period, with data available at 1-min intervals ([NOAA 1998](#)).³ The WRF provides a wind diagnostic for this height, which typically resides between the lowest model level and the surface. However, most available measurements in complex terrain come from the Remote Automated Weather Stations (RAWS) network that employs anemometers mounted closer to the surface (6.1 m AGL) and transmit longer (10 min) averages for the sustained wind once per hour (leaving over 80% of the hour unsampled). Thus, regardless of other factors, contemporaneous and collocated RAWS and ASOS sustained wind reports can be expected to disagree. In verification exercises, adjustments dependent on vertical stability and surface roughness have to be made to the model’s standard 10-m wind diagnostic to avoid a potentially false conclusion of overprediction.

The [WMO \(2010\)](#) notes that “the most difficult aspect of wind measurement is the exposure of the anemometer.” Even a cursory examination of RAWS site photos hosted by the Desert Research Institute (DRI)⁴ reveals numerous examples of problematic anemometer placement with respect to buildings and/or trees. During the aforementioned Witch Creek fire, the RAWS station at Goose Valley (GOSC1) occupied an important location immediately downwind and downslope from the

ignition location, but at the time was closely surrounded by significant obstacles (verified by inspection). It is not known how much larger its event maximum sustained wind (15 m s^{-1}) and gust (25 m s^{-1}) might have been had the station not been sited close to large trees.

Since 2009, SDG&E has deployed surface stations in wind-prone areas across San Diego County ([Fig. 1](#)). Sites were carefully selected in order to accurately and properly gauge the wind threat to well-exposed electrical installations. These stations conform to the RAWS standard ([National Wildfire Coordinating Group 2014](#)) with respect to anemometer height (20 ft or about 6.1 m AGL) and sustained wind formulation (10-min averages from 3-s samples), but report every 10 min instead of hourly. For each 10-min interval, the sample resulting in the largest wind speed is reported as the gust. Station identifiers consist of five characters, terminating with “SD.” (This suffix will be ignored when convenient.)

As a test, SDG&E station GOSSD was purposely placed at a better-exposed location 0.7 km along Black Canyon Road from GOSC1’s original location.⁵ For the month of December 2011, which included several moderate Santa Ana wind events, the 10-min-averaged sustained winds at GOSSD were about 50% stronger than at the more sheltered RAWS station ([Fig. 2](#)), even though they were measured at the same height. Indeed, among the 744 contemporaneous observations of sustained wind during that month, 639 SDG&E observations were larger than their corresponding RAWS wind speed, 48 observations were the same, and only 56 of the RAWS observations (<8% of the total) exceeded the SDG&E reports. As demonstrated clearly below, even closely spaced and well-exposed stations can exhibit wind variability of this magnitude, so part of the GOSSD-GOSC1 discrepancy might have been due to an unappreciated terrain effect. However, this result motivated us to use the SDG&E network exclusively to verify our model results, owing to its high density and optimal siting philosophy. The purpose of our work, after all, is to forecast winds impinging upon electrical lines at risk of igniting wildfires in well-exposed terrain.

b. Model experimental design

The simulations examined herein were made using WRF version 3.5. To represent an operational environment, the model was initialized with the North American Mesoscale Forecast System (NAM) gridded

³ The sampling interval for these stations was shortened from 5 to 3 s between 2005 and 2009 ([Tyner et al. 2015](#)).

⁴ <http://www.raws.dri.edu>.

⁵ Prior to November 2011, GOSSD was sited even closer to GOSC1, in a less well-exposed area intended to mimic the RAWS siting issues ([S. Vanderburg 2012](#), personal communication). GOSC1 was subsequently moved.

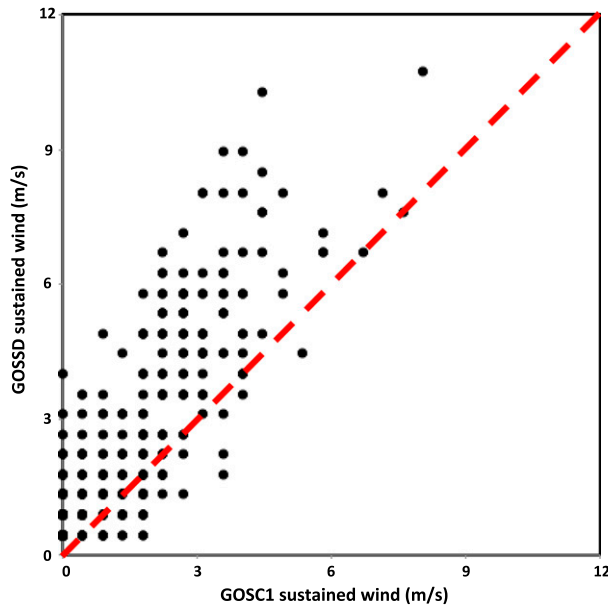


FIG. 2. Scatterplot of hourly sustained winds measured at the Goose Valley RAWs (GOSC1) and SDG&E (GOSSD) sites for December 2011, with a 1:1 correspondence line (red). Owing to rounding, there are numerous overlapping observations.

and 10 PBL schemes as well as 2 land-use databases (USGS and MODIS); for each PBL scheme, the recommended and/or most frequently adopted surface layer parameterization was employed. Simulations were nearly insensitive to some other physics options, such as the microphysics and cumulus schemes (Cao 2015).

The physics combination that consistently best represented the sustained wind observations over a set of events with respect to magnitude and temporal and spatial variation employed the Pleim–Xiu (PX; Pleim and Xiu 1995; Xiu and Pleim 2001) LSM and surface layer scheme, along with the Asymmetric Convection Model, version 2 (ACM2; Pleim 2007a,b) PBL parameterization. This “standard” configuration, labeled PX–ACM2, also utilized the MODIS land-use database, the Rapid Radiative Transfer Model for General Circulation Models (RRTMG; Iacono et al. 2008) radiation parameterization, and explicit horizontal diffusion was not applied. Neither the land-use nor diffusion choice had much impact on the results (Cao 2015) for this combination.

While the physics sensitivity experiment will be explored more fully in Part II, we will also reference herein results using the Noah (Chen and Dudhia 2001; Ek et al. 2003) and thermal diffusion (TD; Skamarock et al. 2008) LSMs, and the Yonsei University (YSU; Hong et al. 2006), Mellor–Yamada–Janjić (MYJ) PBL scheme (Janjić 1994), and total energy–mass flux (TEMF; Angevine et al. 2010) PBL parameterizations. In particular, the Noah–YSU combination, along with the surface layer scheme derived

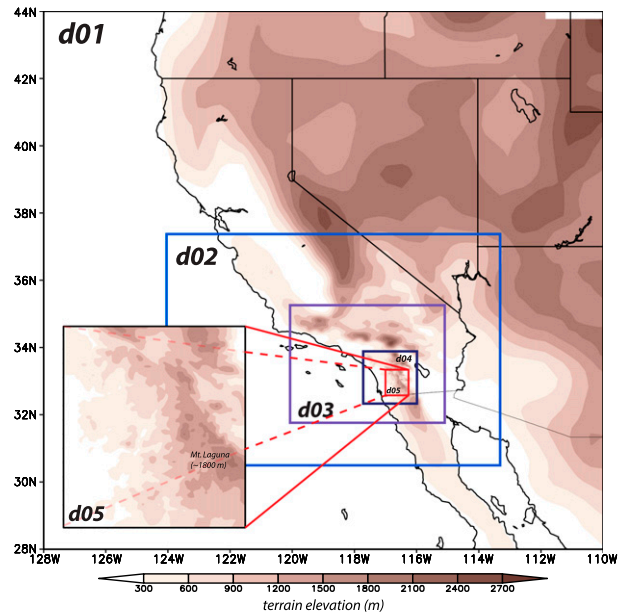


FIG. 3. Domain configuration for the WRF simulations, with topography shaded. Domains 1–5 employ horizontal grid spacings of 54, 18, 6, 2, and 0.667 km over Southern California, respectively. The inset shows an enlarged version of domain 5.

from MM5 (Noah–YSU),⁷ is of interest because it is likely the most commonly used configuration in WRF.

c. Verification strategy

As noted above, SDG&E stations were intentionally placed at wind-prone sites. An unavoidable assumption being made in this study is that the SDG&E stations are representative of the landscape as a whole—or at least as it is rendered in the model. At a given grid spacing, the model is trying to capture the gross features of the terrain, which enter into parameterizations such as the LSM via such factors as the surface roughness length. It cannot directly incorporate subgrid-scale features such as trees, buildings, small hills, and terrain creases that can act to locally modulate the wind in the immediate vicinity of an anemometer. We believe that one advantage of SDG&E observations over their RAWs counterparts is that they are less likely to be influenced by small-scale features that we know we cannot represent on the grid, and thus may be more representative of the landscape we are capable of resolving.

SDG&E mesonet observations were obtained from the Meteorological Assimilation Data Ingest System (MADIS) archive and interpolated to station locations using the Developmental Testbed Center’s MET

⁷ This surface scheme was modified for WRF, version 3.6.

software. For wind, we compared instantaneous model predictions computed on the hour with sustained wind observations, which is the standard (if not often explicitly acknowledged) practice. Comparisons of model winds with observed gusts are not appropriate because the model's resolution, configuration, and filters preclude its ability to resolve small-scale turbulent motions. In theory, model fields could be averaged over time periods comparable to the sustained wind averaging period, but in practice this makes very little difference. The goal is to faithfully capture the overall temporal evolution and spatial characteristics of the event.

WRF computes a wind diagnostic relating the lowest model level wind V_a at height $z = Z_a$ to the WMO standard height of 10 m (V_{10m}) via the logarithmic wind profile assumption (e.g., Oke 1987):

$$V_{10m} = V_a \frac{\ln \frac{10}{z_0} - \psi_{10m}}{\ln \frac{Z_a}{z_0} - \psi_a}, \quad (1)$$

where z_0 is the surface roughness length, and ψ_a and ψ_{10m} represent stability correction functions at Z_a and 10 m that vanish when the surface layer is neutrally stratified. However, proper comparison with the SDG&E network winds requires further adjustment to its anemometer mounting height at 6.1 m AGL level ($V_{6.1m}$), that is,

$$V_{6.1m} = V_{10m} \frac{\ln \frac{6.1}{z_0} - \psi_{6.1m}}{\ln \frac{10}{z_0} - \psi_{10m}}, \quad (2)$$

where $\psi_{6.1m}$ is the stability correction computed at anemometer level.⁸ Although somewhat dependent on the land surface model and surface layer scheme, land-use database (e.g., USGS vs MODIS) employed and season, z_0 values range between 0.05 m and 0.9 m at SDG&E stations, resulting in wind speed reductions of 10%–20% from the 10-m values even when conditions are neutral.

An acknowledged limitation of this study is our assessments are being made solely with near-surface observations and presume a wind profile [Eq. (2)] that is implicitly or explicitly relied upon (e.g., Mass et al. 2002), but not well tested (cf. Stensrud 2007), in complex terrain.

An alternative to the latter would be to shift the vertical coordinate so the lowest model wind level resides at $Z_a = 6.1$ m, permitting a direct comparison with the observations. This has been investigated for a number of events, but we have found that 1) shifting PX-ACM2 did not change its forecast skill very much; 2) PX-ACM2 retained its skill advantage relative to other physics combinations, even after shifting; and 3) most importantly, the shifted PX-ACM2 setup encountered linear instability issues in a subset of events (including the one examined herein) necessitating the use of much smaller time steps. As a consequence, we retain the default Z_a placement for this study. Finally, it is noted that Eqs. (1) and (2) could have been written with the zero-plane displacement modification of the anemometer heights that is sometimes used in areas with significant obstacles; we neglect this adjustment because most SDG&E stations were installed in well-exposed areas.

Event-averaged mean absolute error (MAE) and bias statistics, defined for station j and time i as

$$\text{MAE} = |f_{j,i} - y_{j,i}| \quad (3)$$

and

$$\text{bias} = (f_{j,i} - y_{j,i}) \quad (4)$$

are employed as tools to measure how close pointwise model predictions f_i are to their corresponding observations y_i . Model gridded winds are first interpolated to the SDG&E station locations using hourly information,⁹ representing the initial time and 54 subsequent forecasts. From these data, network averages for each verification time are computed, and the event-averaged MAE and bias represent the mean network average over the 55-h event window. Using these measures, we will show that most model physics configurations generate a high wind bias relative to the observed sustained winds, even after anemometer or model level height adjustment, with the worst offenders ostensibly being those employing the MYJ PBL. However, we discovered the MYJ code was recomputing the 10-m wind values, specifying smaller roughness lengths than actually employed in the model integrations. This purely cosmetic adjustment, shared by the QNSE PBL scheme (Sukoriansky et al. 2006), exacerbated the high

⁸ Neutrality is often presumed when wind speeds exceed about 5 m s^{-1} or so (e.g., Wieringa 1976; Verkaik 2000), which does appear valid among our model simulations. The stability corrections in Eq. (2) were retained for simulations examined in detail in this report, but these was found to have relatively little impact on the results and no influence on the conclusions.

⁹ Mesonet data were obtained at full temporal (10 min) resolution and we elected to replace observed winds on the hour with the largest values reported during the previous 50 min, motivated by the relatively larger high-frequency variability present in the observations and our practical concern with the high wind threat. However, this was found to have relatively little impact on the results and no influence on the conclusions.

wind bias, and removing the code (as done for this study) made physics ensemble members employing MYJ and QNSE much more competitive.

3. The 14–16 February 2013 event observations

Although only moderate in overall strength as a Santa Ana episode, some very impressive winds ($\sim 26 \text{ m s}^{-1}$) and gusts ($\sim 41 \text{ m s}^{-1}$) were recorded in the SDG&E network during the 14–16 February 2013 event. More interestingly, this event was a two-phase episode, with the first phase characteristic of the development of a well-developed hydraulic jumplike feature associated with wind reversals, and the second one being a normal downslope progression of winds.

Certain synoptic-scale conditions interacting with local topography contribute to Santa Ana occurrence (Yoshino 1975; Sommers 1978; Hughes and Hall 2010). This mid-February Santa Ana wind event commenced around 0000 UTC 15 February 2013, as maximum sea level pressures exceeded 1028 hPa in the Great Basin (Fig. 4a), and a midlevel ridge approached the western United States, bringing northeast winds over the mountains encircling Southern California (Fig. 4d). Some stations reported their fastest offshore winds around 1800 UTC 15 February 2013, when the Great Basin high and the 700-hPa ridge reached peak magnitudes (Figs. 4b and 4e). During the next 24 h, the high pressure migrated eastward (Fig. 4c), away from Southern California, the surface offshore winds weakened, and the 700-hPa ridge flattened (Fig. 4f).

Figure 5 presents the maximum wind gusts observed in the SDG&E network for the event. The strongest gusts are found to be located along the western slopes, close to but not at the ridgelines. The great spatial variability of the winds can be detected in Fig. 5b, which focuses on the “central area” that comprises the stations of greatest present interest. Peak gusts varied between 10 and 30 m s^{-1} within a 5-km distance, suggesting each station is representative only of a small local area, at least with respect to the winds. The event-maximum sustained winds (not shown) are similar in pattern although naturally weaker in magnitude.

Figure 6a presents a time series of winds and gusts recorded at central area stations Sill Hill (SIL) and Boulder Creek (BOC). The event as a whole was characterized by two peaks separated by a protracted lull that occurred during the afternoon and early evening hours of 15 February. At 1830 UTC (1030 PST) on 15 February, SIL recorded a 41 m s^{-1} wind gust, at a time when no other stations in this region had a gust exceeding 26 m s^{-1} . Indeed, the winds were

50% weaker at BOC, which is just 1.6 km to the south (Fig. 5b). (Keeping in mind that the sustained wind represents 10-min averages and the gusts are single 3-s samples, note how similar the sustained wind at SIL is to the wind *gusts* from BOC.) It would be easy to dismiss such a high wind observation, but the station record shows that gusts exceeding 36 m s^{-1} were frequently recorded occurrence (Fig. 6a), and eye-level gusts of 33 m s^{-1} had been measured with hand-held anemometers at the site about an hour earlier (B. D’Agostino and S. Vanderburg 2013, personal communication). A close inspection of the topography in the vicinity of SIL and BOC (not shown) indicates that SIL is sited on a small local ridge while BOC resides in a narrow terrain crease, very small-scale features that may be relevant to the wind speeds and exposures and illustrate the challenge that is faced in simulating and verifying the winds across this area.

We now shift focus to the Witch Creek (WCK) area, where the SDG&E station density is particularly high (Fig. 5b). At West Santa Ysabel (WSY; Fig. 6b), located on the west-facing slope about 9–10 km down from the ridge, gusts during the first phase peaked at 26 m s^{-1} at 1800 UTC (1000 PST) on 15 February and regained comparable strength by midnight local time before finally slowing as the event wound down. Although about 40% weaker than the gusts, the sustained winds at WSY followed a similar trend. At SDG&E station Julian (JUL), close to the ridge, the gusts were much weaker than WSY’s during the first phase, stronger (although still fairly slow) during the afternoon lull, and markedly weaker again during the second phase. This hints that there is something structurally and/or dynamically different about the second half of the event.

The winds also behaved very differently at the WCK station (Fig. 6c), which is less than 5 km downslope from WSY. Through the first phase, WCK’s gusts remained much weaker than WSY’s. Note the wind direction at WCK occasionally reversed to upslope (at times indicated by the black dots) during this period, including at and around the time of WSY’s peak gusts. During the lull between the two phases, the WSY and WCK winds were comparably weak. While the winds remained downslope at WCK during the lull, they often reversed to upslope at WSY (at times indicated by the gray squares). Wind reversals reappeared at WCK during the onset of the second phase before downsloping became firmly reestablished there. WCK recorded its event maximum gust of 23 m s^{-1} at 1130 UTC 16 February, during the second pulse and about 3 h after the winds at WSY started to decline.

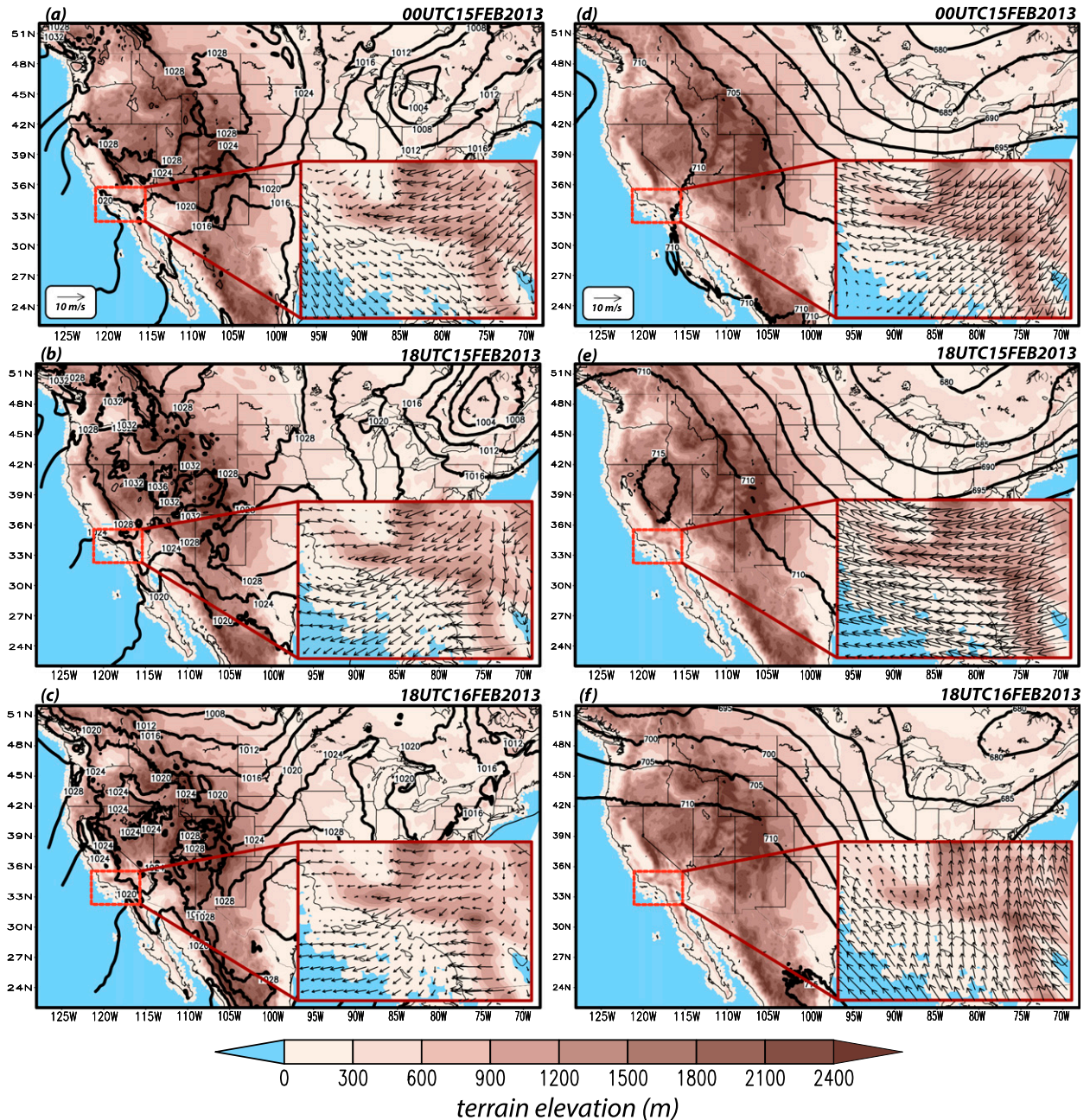


FIG. 4. NAM model sea level pressure analyses for (a) 0000 UTC 15 Feb, (b) 1800 UTC 15 Feb, and (c) 1800 UTC 16 Feb 2013; and 700-hPa analyses for (d) 0000 UTC 15 Feb, (e) 1800 UTC 15 Feb, and (f) 1800 UTC 16 Feb 2013. The insets show the total (left) 10-m and (right) 700-hPa winds of Southern California (the red box). Only a subset of vectors are plotted for clarity. Topography is shaded.

Station Sunset Oaks (SSO) is located 7 km farther downslope from WCK. Note that, during the first pulse, its gusts were weaker than, but in phase with, WSY's. The wind reversals at WCK during this time occurred with while downslope flow was observed both uphill (at WSY) and downhill (at SSO), indicating a rotor or jump may have formed there. The upslope shift of the wind reversals during the lull

period from WCK to WSY could be explained by a change in the rotor or jump position. Station SSO emerged last from the lull, and its second peak was reached after the gusts at both WSY and WCK had started to decline. Taken together, these suggest a two-part Santa Ana event in which winds were largely in phase early in the event, apart from the suspected jump at WCK, and had a second pulse

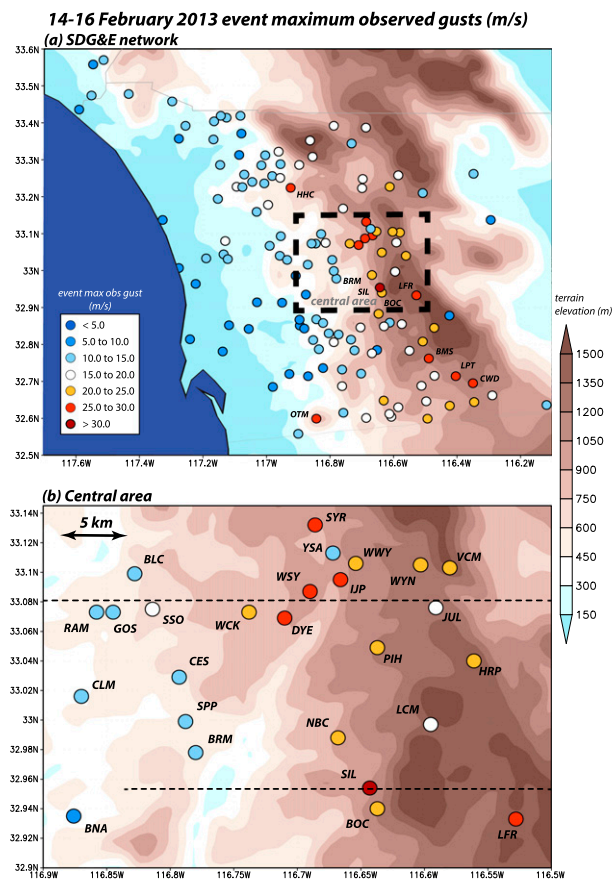


FIG. 5. Spatial distribution of 14 Feb 2013 event maximum observed wind gusts (m s^{-1}) with topography (shaded) for SDG&E stations in (a) the entire network and (b) the central area identified in (a). Black dotted lines denote locations of cross sections across WSY and SIL shown in Figs. 13 and 15.

consisting of a marked downslope progression as the overall winds abated.

4. Model simulations and verifications

In sections 4a–c, the standard run is verified and examined, and its configuration is justified.

a. Verification of the standard run

To a large extent, the standard PX–ACM2 simulation captured the magnitude and temporal evolution of the SDG&E network-averaged sustained winds (the mean of 138 sites), at least after the first 12 h (Fig. 7). Over the entire simulation period, the linear correlation between the network-averaged hourly observations and forecasts was 0.85, and the network- and event-averaged MAE and bias were 2.23 and 0.07 m s^{-1} , respectively. Individual stations having relatively large and small errors or biases are ostensibly dispersed randomly in space (Fig. 8). Like the network as a whole, the spatially

averaged bias is nearly zero in the aforementioned central area, although clearly very variable in space (Fig. 9), so that overpredicted stations reside in close proximity to underpredicted ones. This hints at the value of high network density and the danger of drawing conclusions from a limited number of stations.

However, these plots may obscure some potentially important aspects of the sustained wind reconstructions. Among the 138 stations employed in the verification, MAE is positively correlated with the event-averaged observed wind (Fig. 10a; $R^2 \sim 0.5$ for the red curve) while the bias is negatively related (Fig. 10b; $R^2 \sim 0.5$ for the red line) to the wind. Both of these relationships are largely driven by the stations recording the highest wind speeds, and are much smaller ($R^2 \sim 0.1$ and 0.2 , respectively), although still significant at the 99% level, if the windiest 10 locations (7% of the network) are removed. The uniqueness of the windy station subset can be seen when MAE and bias are presented in rank order (Figs. 10c,d); the majority of the locations (indicated by the red dots) comprise the blades of hockey stick–like structures. Six of these high-wind stations (SIL, LFR, VCM, BOC, HRP, and IJP) reside in the central area (Fig. 9).

Still, if the windiest locations are excluded, the network- and event-averaged MAE and bias are only slightly changed (to about 2.1 and 0.4 m s^{-1} , respectively). Furthermore, we will show later (in section 4c) that this result is a common characteristic of Santa Ana WRF simulations overall, independent of model physics and not unique to this event, so that exclusion of the windy subset would not alter our findings. Instead, it does not appear possible to accurately predict the winds at the windiest locations without simultaneously overpredicting the wind speed nearly everywhere else. The standard model configuration was selected to maximize network-averaged skill at reproducing the 6.1-m wind integrated over the network and through the event (as well as through other episodes not explicitly considered herein). It needs to be borne in mind that the model will require bias correction at the most wind-favored locations.

b. Spatial and temporal variation of the winds in the standard run

Figure 11 (left column) compares hourly time series of simulated sustained wind at stations WSY, WCK, and SSO, with the observations used in the verification. Overall, the simulation captures the evolution and magnitude of the winds at each station to a good degree, although there are some clear timing issues. At WSY, the magnitude of the second pulse was underpredicted, although the phasing was skillful (Fig. 11a). The second phase’s winds ramped up too early at both

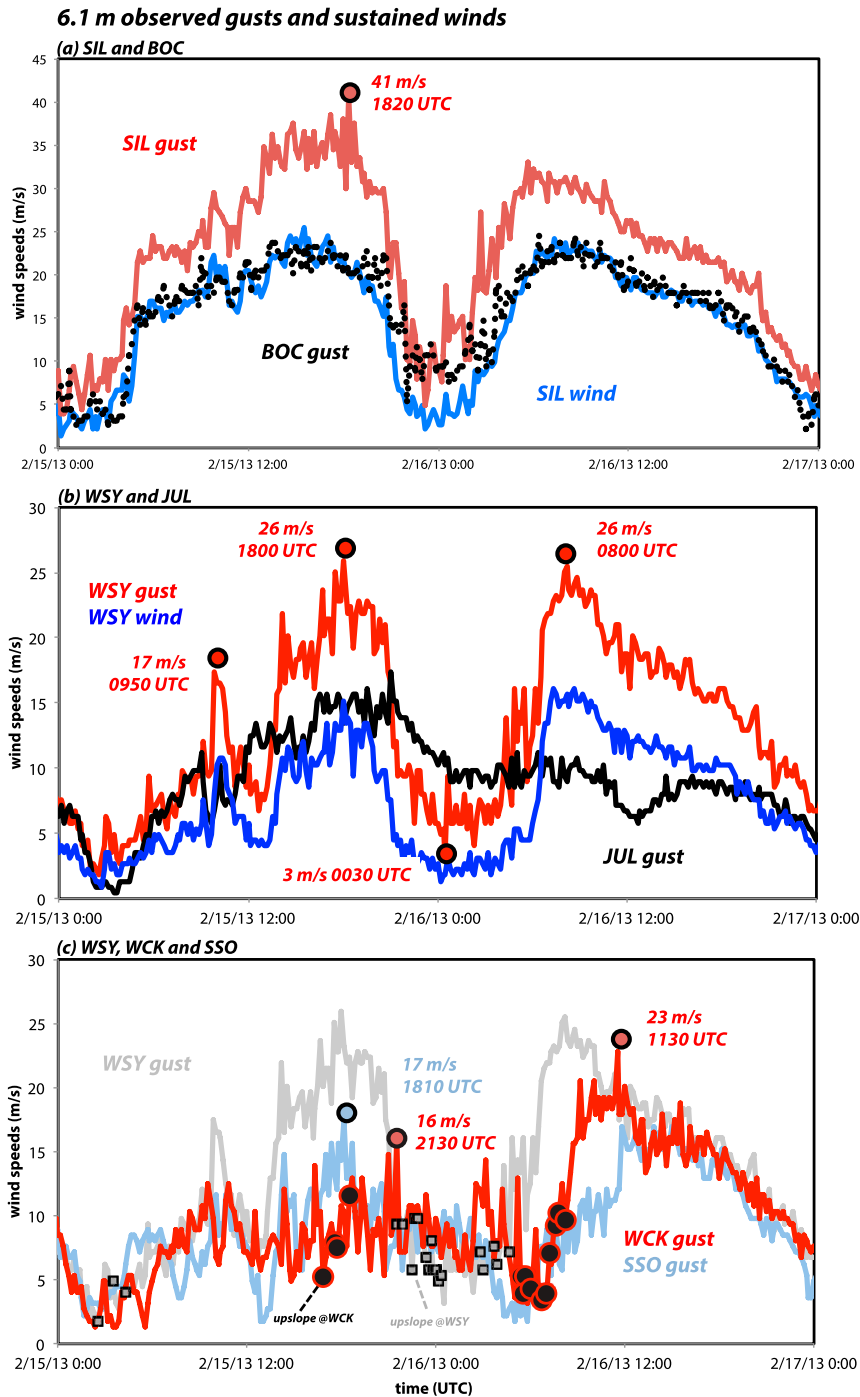


FIG. 6. Time series of observed gusts and sustained winds (m s^{-1}) over 2 days at (a) SIL and BOC; (b) WSY and JUL; and (c) WSY, WCK, and SSO. Some maxima and minima are highlighted. In (c), black dots indicate times when winds were directed upslope at WCK and gray squares indicate times when winds were directed upslope at WSY.

WCK and SSO (Figs. 11b and 11c). That said, however, the model captured the overall event evolution (Fig. 11d) as manifested by the observed winds (Figs. 11a–c) and gusts (Fig. 6c): during the first pulse,

wind speeds remained markedly weaker at WCK than at stations both upslope and downslope, and the second pulse was characterized by a downslope progression of the flow with time.

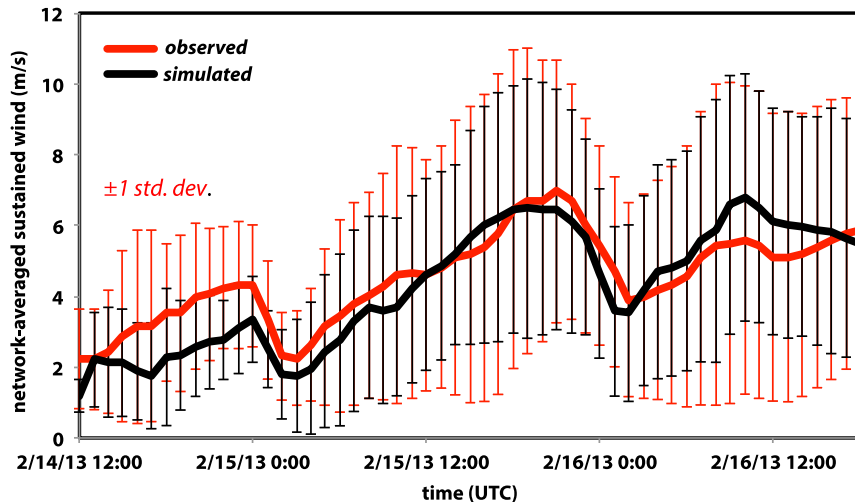


FIG. 7. Time series of SDG&E network-averaged sustained wind (m s^{-1}) observations (red line) at 6.1 m AGL over 2 days, for comparison with predictions from the standard (PX-ACM2) run (black line). Red and black color bars are plus and minus one standard deviation for observations and the standard run, respectively. The plot spans the entire 54-h simulation period.

Having demonstrated reasonable fidelity with the available observations, the simulation will be used to complete the horizontal wind field (Fig. 12), and provide insight into the vertical dimension that is missing from the observations (Figs. 13 and 15). By 0800 UTC 15 February 2013 (Fig. 12a), the downslope windstorm had already started, but the winds near the ground at WSY and stations farther downslope had not yet begun to rise. The model indicates that significant easterly flow was already present above WSY and WCK, but had not yet reached the surface (Fig. 13a). Recall that by 1740 UTC, winds recorded at WSY and SSO had reached their first-phase peaks, but WCK's winds remained quite weak (Figs. 6c and 11b). The simulation has indeed developed a jumplike feature almost directly above WCK at this time (Fig. 13b), rendering relatively weak winds there and upslope nearby (see the square and blue arrows in Fig. 12b). The reversed upslope winds indicate the existence of a local horizontal roller and characterize a turbulent and clearly defined hydraulic jump (e.g., Chanson 2009). Note also that, as expected, the wind speeds had not strengthened very much at JUL, which is located at the top of the ridge and at the very edge of the terrain-induced flow amplification.

Five hours later, there was a brief period (around 2130 UTC) during which the observed gusts at WCK were actually stronger than at the other stations (Fig. 6c), having reached their first-phase peak of 16 m s^{-1} . The winds at WSY and SSO had already entered the lull period, and the wind at WSY was directed upslope at and after this time. While the timing is not perfect, the model suggests this occurred as the jumplike

feature retreated upslope, relocating the reversed flow to WSY (Fig. 13c; see square in Fig. 12c). As the windstorm subsequently retreated even farther eastward, it also weakened and became more elevated (Fig. 13d). The model reveals that strong near-surface winds still existed during the lull, but became concentrated close to the ridge and in an area where there were no stations (see between WSY and JUL in Figs. 12d and 13d).

The second phase of the Santa Ana event ensued as the reintensifying flow began progressing downslope again after 0500 UTC 16 February (Figs. 13e and 12e). Note another, smaller-amplitude jump formed in the vicinity of WCK, again consistent with the wind reversals seen in the observations (Fig. 6c). By midnight local time (0800 UTC), however, that feature had disappeared and the downsloping flow became “flatter” and, eventually, shallower as the Santa Ana event eventually wound down (Figs. 13f–h). The observations indicated that a westward and downslope progression in the peak near-surface wind speeds (Fig. 6c) had occurred, and the model has largely captured this behavior (Figs. 11d and 12f–h).

The retreat separating the two phases likely responds, at least in part, to temporal variations upstream of the mountain ridge, some of which are diurnal in character and some are associated with the evolution of the synoptic-scale environment. Figure 14 presents a time versus height view of stability and temperature (at top) and winds (at bottom) at the location marked “E” in Fig. 13, just east of the ridge. The figure reveals that an elevated inversion atop a less

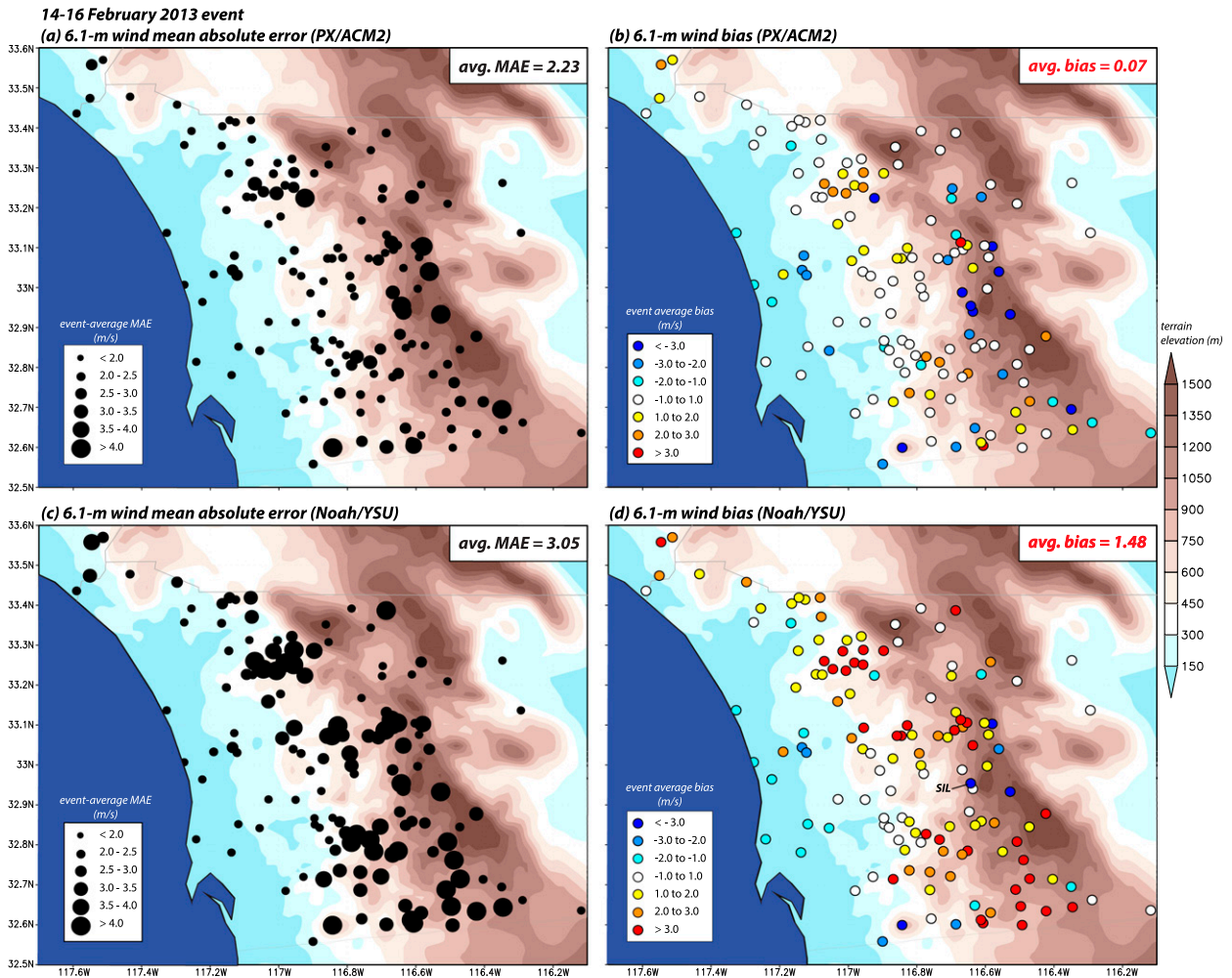


FIG. 8. As in Fig. 5a, but for (a) event-mean sustained wind MAE against observations and (b) event-mean sustained wind bias against observations, for the standard simulation. (c),(d) As in (a),(b), but for the Noah-YSU run.

stable layer was present through most of the Santa Ana episode, similar to the situation studied by Vosper (2004). Elevated inversions also occur during high-wind events at Boulder, Colorado (e.g., Brinkmann 1974; Klemp and Lilly 1975). The inversion had appeared prior to 0000 UTC 15 February, and the winds just east of the ridge had already acquired an easterly component, but the simulated winds at WSY (superposed for reference) did not rise until the inversion and cross-ridge flow both strengthened during the next 12 hours.¹⁰

¹⁰ A critical level with respect to the cross-ridge wind appeared above 4 km above mean sea level (MSL) prior to WSY's first peak, but did not persist. A mean state critical level was present at 7 km MSL throughout the event; not shown.

After the maximum winds were reached at WSY, note that the easterlies above point E subsequently changed relatively little through 0600 UTC 16 February, spanning the entire interperiod lull. While a closer examination is required, the windstorm's upstream retreat appears to be associated with the erosion and descent of the inversion that occurred after 1800 UTC on the 15th, in the hours after sunrise (around 1430 UTC). Part of this evolution is a consequence of daytime heating, which is evident in the evolution of the temperature contours below about 3.5 km MSL (2.4 km AGL) in Fig. 14a. The increasing separation between the 298- and 306-K isentropes in Fig. 14b during this time is also consistent with surface-based heating, and indicative of a weakening and repositioning of the inversion.

The second phase commenced after the inversion again ascended after 0400 UTC 16 February, a few hours after sunset (around 0130 UTC). Through the second

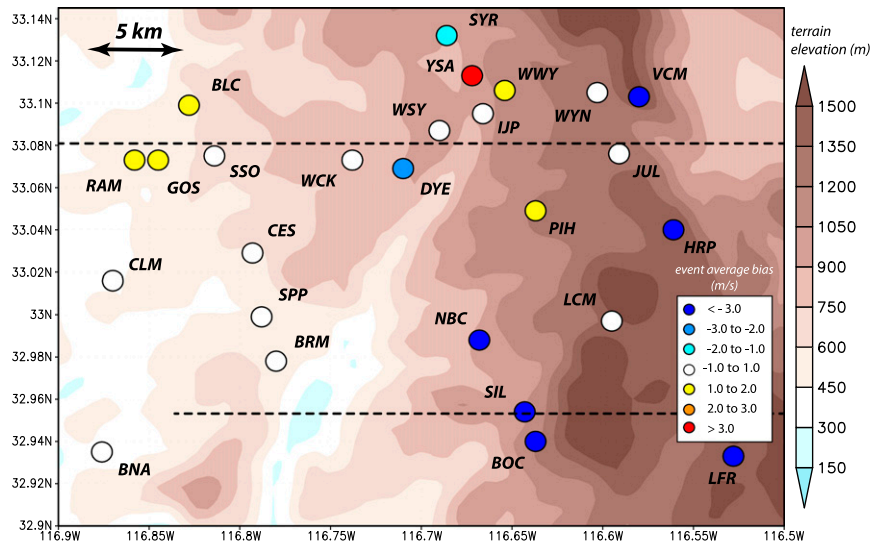


FIG. 9. As in Fig. 8b, but zoomed into the central area. Labels indicate names of SDG&E stations, with the “SD” suffix omitted. Black dotted lines denote cross sections across WSY and SIL shown in Figs. 13 and 15.

pulse, however, the easterly winds were not only weaker but also located closer to the surface, and the stability structure evolved further, becoming surface based after sunrise on 16 February as the simulated downsloping winds became shallower (Figs. 13g,h). This shift in the stability structure, which appears to reflect the evolving large-scale environment, may explain the different character of the downslope winds during the two phases. Vosper (2004) and Durran (1986) have demonstrated that the structure and intensity of windstorms can be very sensitive to even subtle shifts in characteristics such as inversion height and stable layer depth.

Figure 15 switches focus to the west–east vertical cross sections across SIL (see Fig. 12a), the focus of Fig. 6a. During the first phase of the event (Figs. 15a–d), the downslope winds were not able to progress beyond this station, at least at this latitude, prior to the afternoon retreat upslope. It is recalled that SIL’s observed peak gust (41 m s^{-1}) occurred at 1820 UTC (Fig. 6a), the time of Fig. 15c. The winds extended farther downslope during the second pulse, fitfully forming jumplike features (Figs. 15e–g) in areas lacking stations (e.g., between BRM and SIL in Figs. 12e–g). The event winds waned more quickly in this portion of the central area than the subzone around WCK (Figs. 12h and 15h).

As seen earlier, SIL and BOC were among the most severely underpredicted sites (Fig. 9). Reconstructions for these two stations are very similar (Fig. 11e), which is unsurprising due to their small separation (1.6 km) relative to the 667-m resolution of D5. A nearby station, North Boulder Creek (NBC), was also underpredicted

(Fig. 11f), with a delayed windstorm onset, although the model accurately captured the fact the NBC site was less windy than both SIL and BOC. At Barona Mesa (BRM), located farther downslope (Fig. 9), both the simulated and observed winds remained generally weak during the episode (Fig. 11g), suggesting that the model’s rendition of the spatial extent of the strong winds is reasonable.

c. Justification of the standard configuration

Our standard configuration employs a sub-1-km nest placed over the heart of the SDG&E network. It is well appreciated that terrain gap and downslope flows are significantly modulated by the shape of the topography, which is in turn dependent on the resolution of the model grid and the topographic database. Horizontal resolution sensitivity is demonstrated using vertical cross sections taken west–east across station WCK for PX–ACM2 simulations employing horizontal grid spacings between 667 and 10 km (Fig. 16). The fields shown are 4-h averages taken between 1500 and 1900 UTC 15 February, straddling the peak of the event’s first phase at WSY (Fig. 6b), and network- and event-averaged bias and MAE are also reported.

The previously noted jump over WCK (Fig. 13b) is revealed to be a persistent feature in the highest-resolution run (Fig. 16a), which also has the smallest bias and MAE of the four simulations shown. Although it does not capture the jump, the 2-km simulation (Fig. 16b) does resemble a spatially smoothed version of the 667-m run’s flow, and the strongest winds are still correctly positioned near station WSY. Further resolution

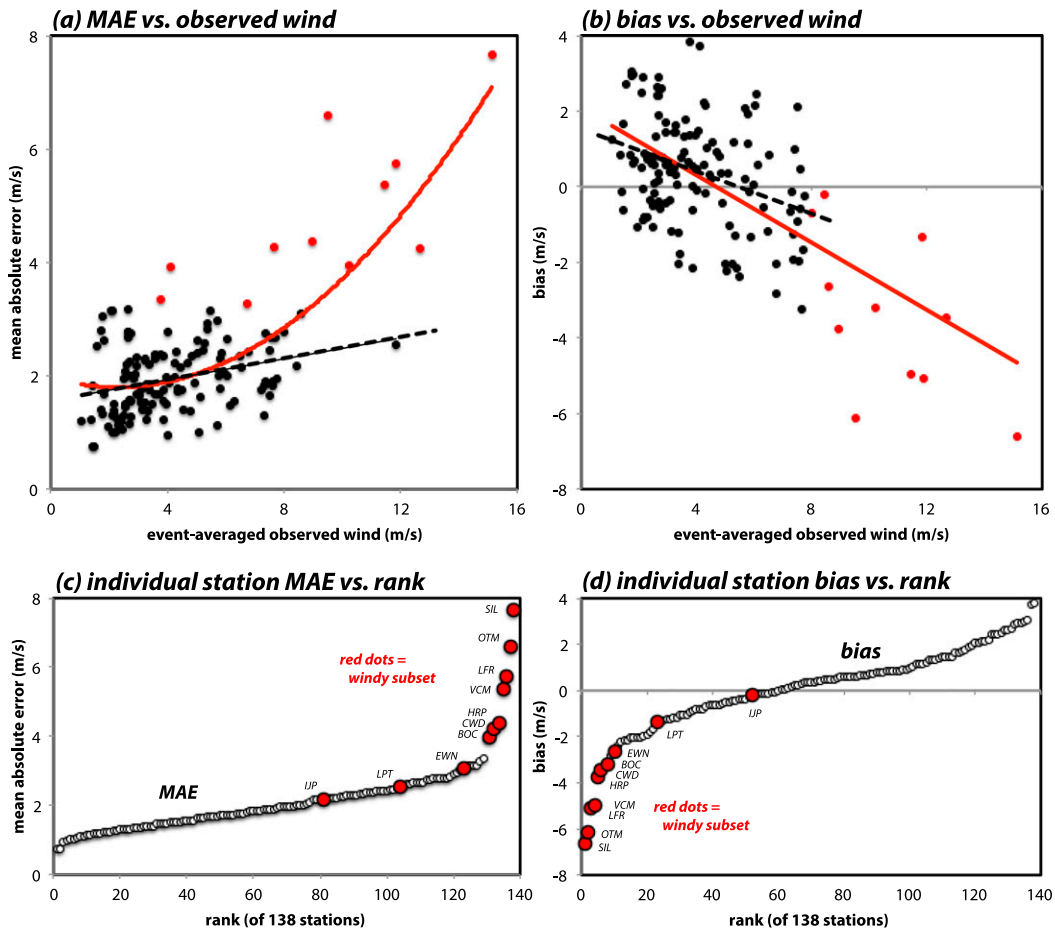


FIG. 10. (a) Scatterplot of event-mean observed wind vs MAE in the PX-ACM2 simulation for the 138 SDG&E stations. Red points identify the 10 windiest stations (see text). Least squares fits including all stations are shown in red, and those including only the black points are shown in black. (b) As in (a), but for event-mean observed wind vs mean bias. (c) Station MAE shown in rank order, with red points again identifying the windiest stations (identified by name). (d) As in (c), but for bias.

degradation, however, profoundly alters the shape of the terrain and improperly changes the location and horizontal extent of the maximum winds, leading to larger MAEs and sizable high wind biases (Figs. 16c,d). (Recall from the introduction that operational models tended to push high winds too far down the slope too often; clearly lower resolution can contribute to that.) Based on these results, it is concluded that 2-km resolution is acceptable but wider grid spacing cannot reliably place the fastest winds at the most likely correct locations. We elected to deploy a sub-1-km domain within the SDG&E mesonet to capture relatively subtle features such as the narrow northeast-southwest-oriented canyon immediately east of WSY and the terrain depression near WCK that can be seen in Fig. 16a.

As mentioned earlier, PX-ACM2 was selected for the standard run owing to its small MAE and nearly zero bias for the event-averaged sustained wind, in this as

well as other cases (cf. Cao 2015, and below). Nearly all other physics combinations resulted in a positive wind bias as well as larger MAE for this event (Fig. 17). The members have clearly clustered with respect to LSM, with the choice of the PBL scheme having only a secondary effect (especially after the cosmetic MYJ-QNSE fix; see section 2c). For a given LSM, we have often found the largest error to be associated with the TEMF PBL parameterization, as also occurred in this experiment. This is believed to be another cosmetic result, being a consequence of TEMF's surface layer scheme not incorporating stability corrections [ψ in Eq. (1)] into its near-surface wind diagnostic, thereby rendering it slightly less competitive relative to the alternatives. Keep in mind that these winds have been adjusted to the 6.1-m level; a straight comparison with the model's 10-m wind diagnostic would have suggested even larger overpredictions.

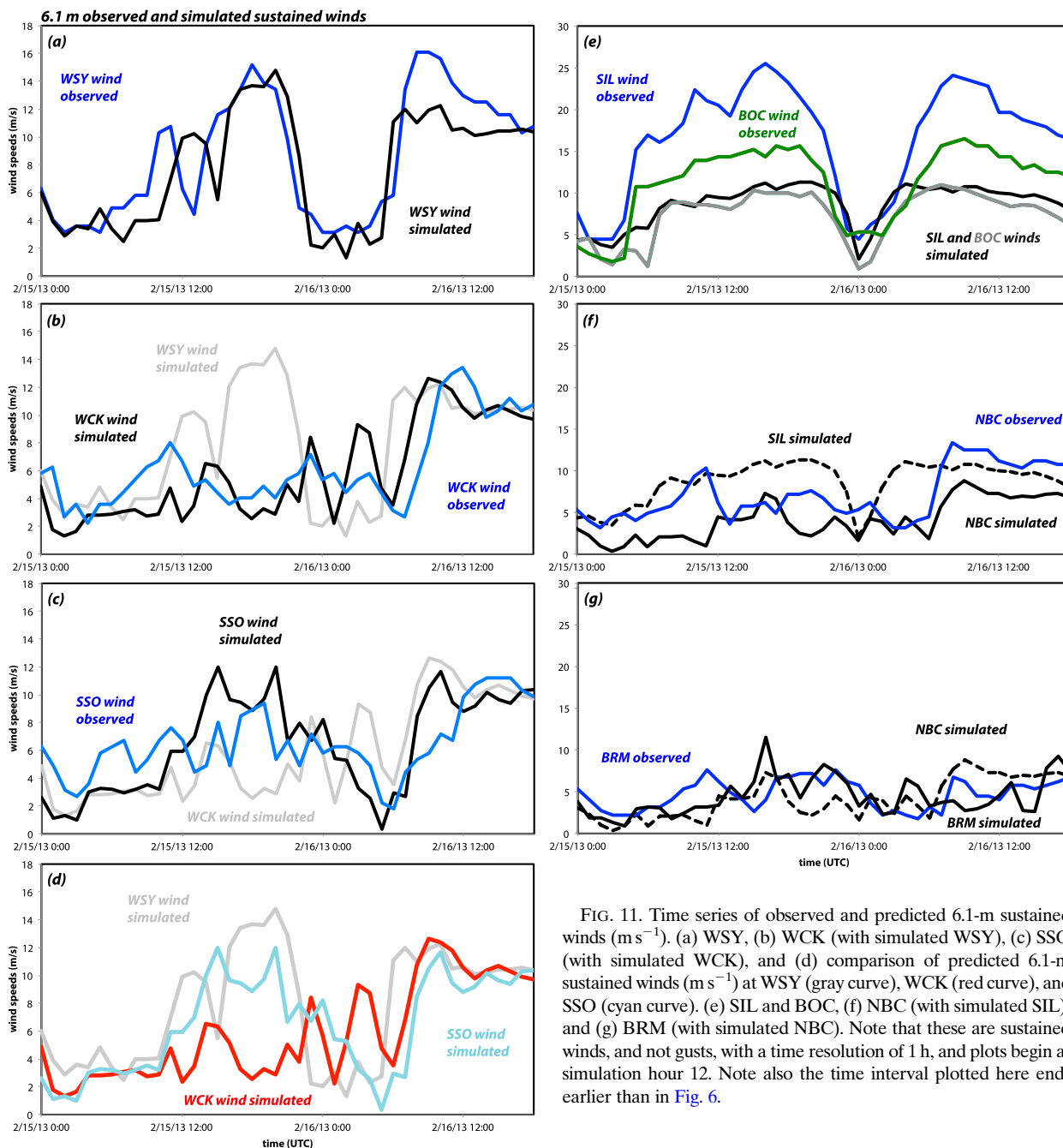


FIG. 11. Time series of observed and predicted 6.1-m sustained winds (m s^{-1}). (a) WSY, (b) WCK (with simulated WSY), (c) SSO (with simulated WCK), and (d) comparison of predicted 6.1-m sustained winds (m s^{-1}) at WSY (gray curve), WCK (red curve), and SSO (cyan curve). (e) SIL and BOC, (f) NBC (with simulated SIL), and (g) BRM (with simulated NBC). Note that these are sustained winds, and not gusts, with a time resolution of 1 h, and plots begin at simulation hour 12. Note also the time interval plotted here ends earlier than in Fig. 6.

The commonly employed Noah–YSU combination resided in the middle of our 48-member physics ensemble (Fig. 17), with obviously larger MAE at most stations (Fig. 8c). While SIL was still substantially underpredicted (Fig. 8d), over three-quarters of the sites had a positive wind bias (Fig. 18b). We note that this Noah–YSU run’s bias and MAE were comparable to PX–ACM2’s values from its 6-km run (see Fig. 16c).

Earlier, we demonstrated (Fig. 10) that while the network-averaged bias was nearly zero, the standard PX–ACM2 simulation’s bias (and MAE) were functions of observed event-average sustained wind speed, driven primarily by a handful of particularly windy locations. Figure 18, which compares the PX–ACM2 configuration with two others, Noah–YSU and TD–TEMF, for the present as well as two other strong Santa Ana wind episodes, shows this tendency is a common occurrence. For

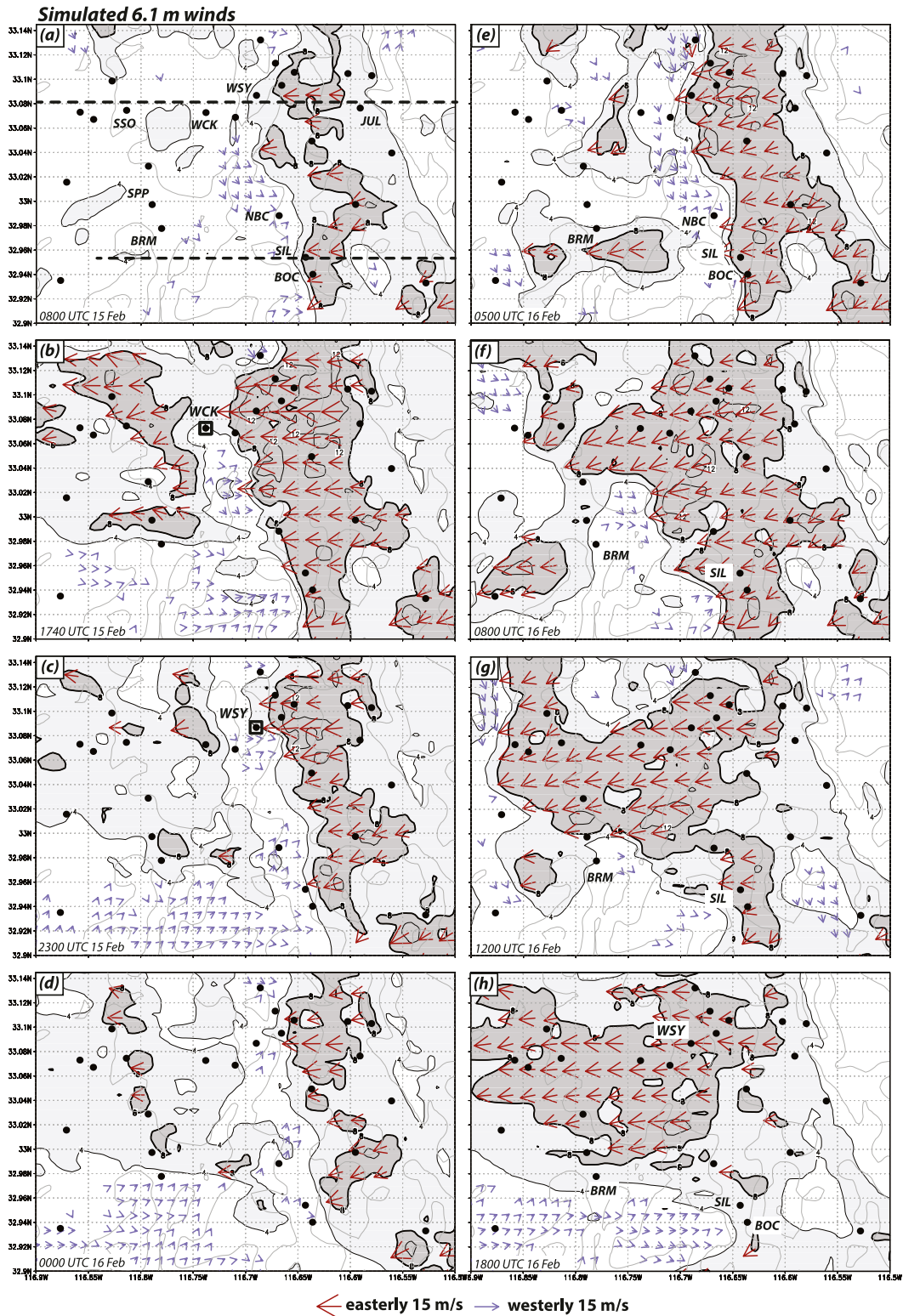


FIG. 12. Simulated 6.1-m horizontal wind speed (4 m s^{-1} interval, 8 m s^{-1} contour bolded) for (a) 0800 UTC 15 Feb, (b) 1740 UTC 15 Feb, (c) 2300 UTC 15 Feb, (d) 0000 UTC 16 Feb, (e) 0500 UTC 16 Feb, (f) 0800 UTC 16 Feb, (g) 1200 UTC 16 Feb, and (h) 1800 UTC 16 Feb 2013, with topography (300-m gray contours). Black dots denote SDG&E surface stations. Dashed lines in (a) denote locations of vertical cross sections shown in Figs. 13 and 15. Blue arrows denote winds with a westerly component $\geq 0.5 \text{ m s}^{-1}$, and red arrows denote winds with an easterly component $\geq 8 \text{ m s}^{-1}$. Many vectors are omitted for clarity.

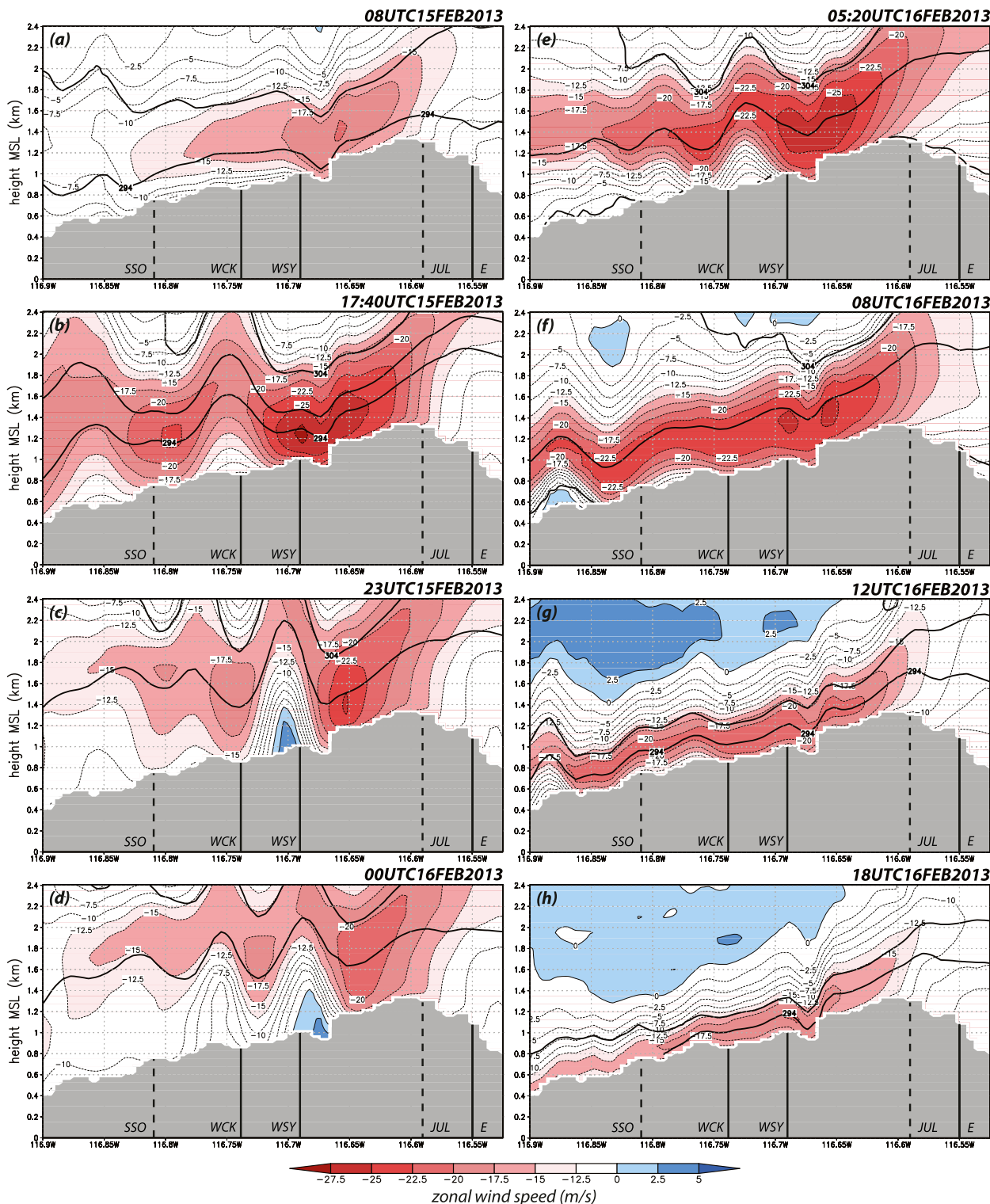


FIG. 13. Vertical cross section of zonal wind speed (shaded, with 2.5 m s^{-1} interval thin contours), taken west-east across WSY with underlying topography in gray (see Fig. 12a). Thick contours denote isentropes (5-K interval). Approximate locations of stations JUL, WSY, WCK, and SSO are marked. WCK, SSO, and JUL are displaced somewhat from the vertical plane depicted. The location for Fig. 14 is marked ‘E.’

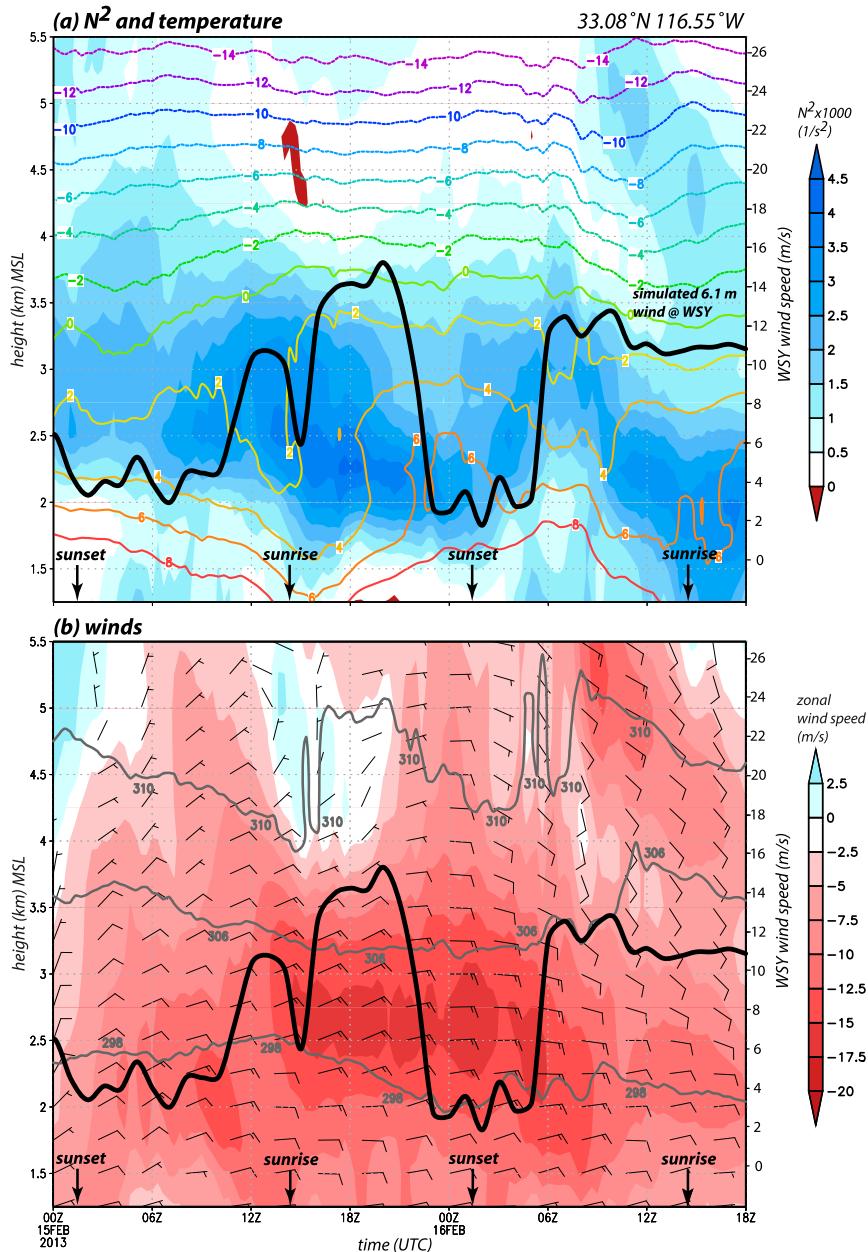


FIG. 14. Time–height plot of simulated (a) stability (dry squared Brunt–Väisälä frequency N^2 , shaded as indicated) and temperature (2°C contours); and (b) zonal winds (shaded as indicated), horizontal wind barbs (in m s^{-1}), and selected potential temperature contours (298, 306, and 310 K) for location marked “E” in Fig. 13. Simulated sustained winds at WSY from Fig. 11a superposed for convenience; scale at right. Note that the plot does not start at model initiation time and fields have been vertically interpolated and thus wind barbs do not necessarily correspond to model levels.

PX–ACM2, aggregation of the three events still yields a roughly zero network-average bias, whether or not the windy subset is removed. The other two configurations, however, tend to have larger biases (e.g., TD–TEMF overpredicts the wind at over 80% of the stations among the three events) even before the windiest stations are removed, as well as larger spreads.

5. Discussion and summary

We have examined the 14–16 February 2013 Santa Ana event, which possessed many characteristics of a moderately intense downslope windstorm on the west-facing slopes of San Diego County, as part of an effort to improve wind forecast skill in this area. This study was made possible by observations from the San Diego Gas

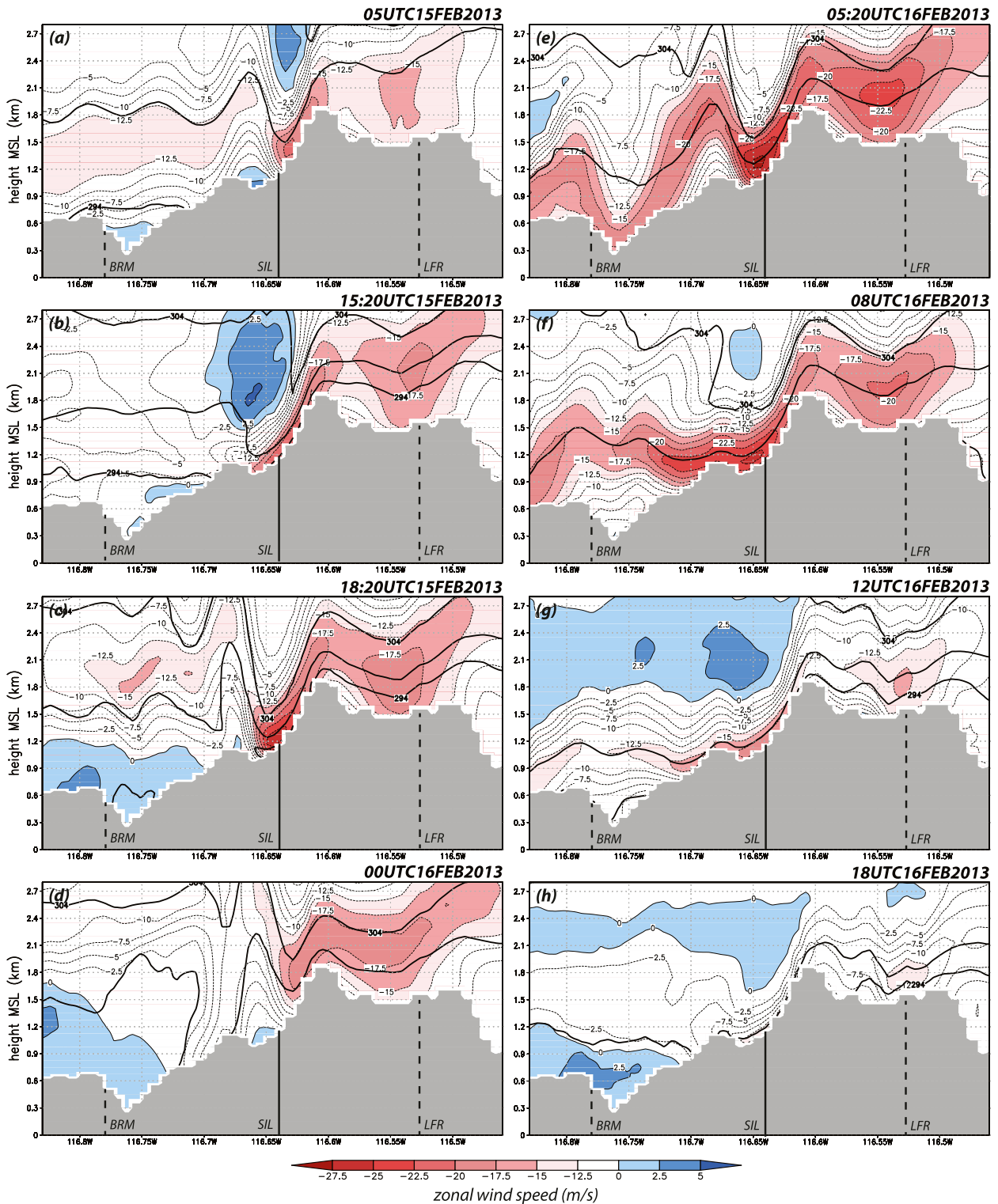


FIG. 15. As in Fig. 13, but across station SIL. Note that some times do not match those in Figs. 13a-h.

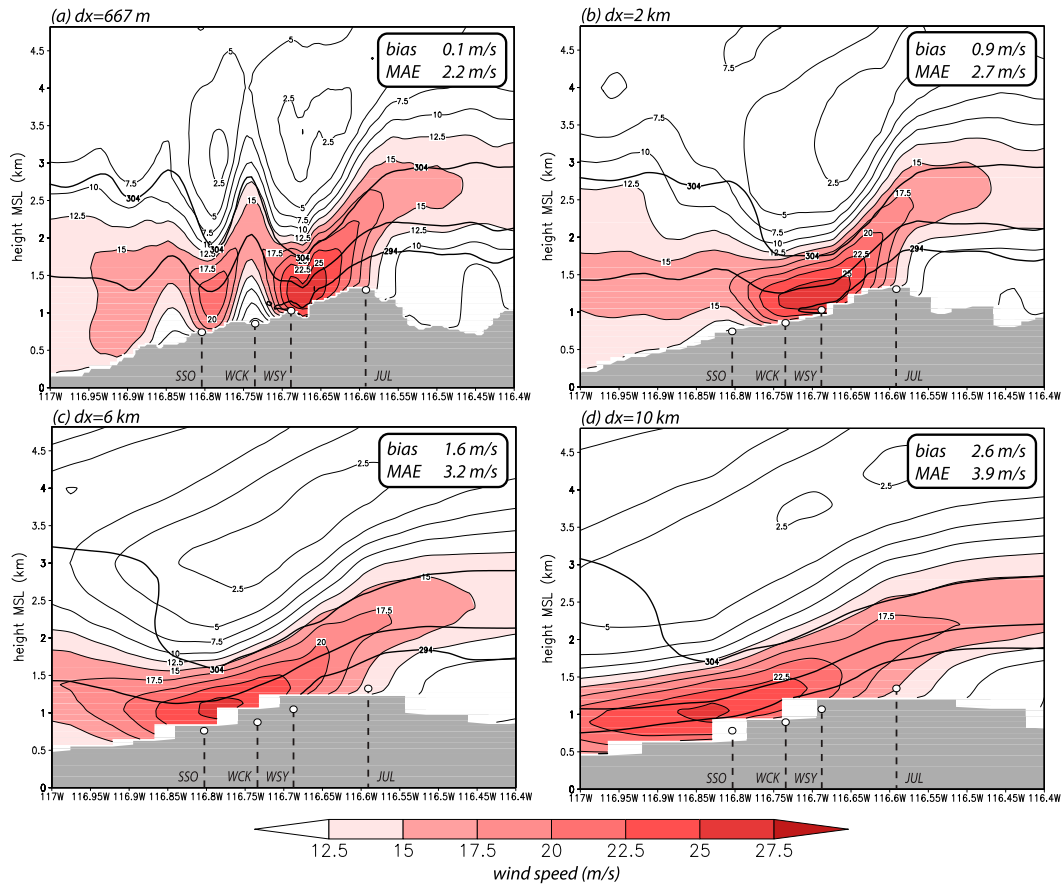


FIG. 16. Vertical cross sections of 4-h averaged horizontal wind speed (2.5 m s^{-1} contours and red shaded fields) for 1500–1900 UTC 15 Feb 2013, taken west–east across Witch Creek for the (a) 667-, (b) 2-, (c) 6-, and (d) 10-km horizontal grid spacing simulations. Thick black contours are the 294-, 299-, and 304-K isentropes. Gray shaded area depicts topography. The network- and event-averaged sustained wind MAE and bias are given in the box. The local rise in topography around 116.5°W longitude in the 2-km rendition results from a nearby topographic feature encroaching into the plane depicted owing to smoothing.

and Electric (SDG&E) mesonet, an unprecedented dense, homogeneous, and reliable observation network of ~ 140 stations sited in wind-prone areas, especially in the mountainous backcountry of San Diego County. These observations revealed that the 14–16 February 2013 Santa Ana episode consisted of two pulses separated by a protracted lull, and suggested that the first phase possessed a hydraulic jumplike flow in part of the network, while the second was characterized by a clear downslope progression of the winds with time as the event itself wound down.

The motivation of this study was to improve wind forecast skill in the area, and the WRF was selected for this effort. WRF provides many PBL and land surface parameterizations, permitting a very wide range of model configurations, many of which were tested for this and other recent Santa Ana wind events. Simulations were verified against SDG&E sustained wind observations,

and the principal tools employed were the mean absolute error (MAE) and bias (mean error), averaged over the event at each station, and also averaged over the entire network. For this and other events, the Pleim–Xiu LSM with the ACM2 PBL scheme (PX–ACM2) combination performed well, typically minimizing MAE with a nearly zero bias with respect to the sustained wind when averaged over the network and event.

Telescoping nests were used with horizontal grid spacing of 2 km over San Diego County and 667 m over the county's highest terrain. While the 667-m grid permitted the model to capture the observed jumplike flow feature during the first pulse that was missing in the 2-km simulations, it otherwise had little influence on the network-averaged verification statistics. Horizontal resolution coarser than 2 km, however, exaggerated the spatial extent of the downslope flow, resulting in higher wind biases. Resolution also influences how well models

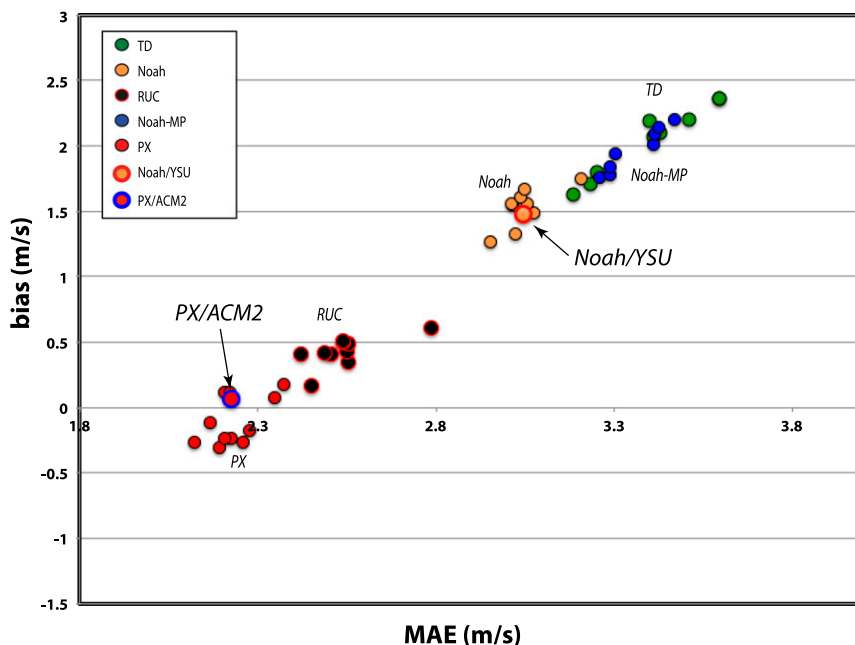


FIG. 17. Scatterplot of network- and event-averaged 6.1-m sustained wind bias vs MAE (both m s^{-1}) from the 48 physics ensemble members for the 14–16 Feb 2013 episode, color coded by LSM. For each PBL scheme, the recommended and/or most frequently adopted surface layer parameterization was employed. For members using the MYJ PBL scheme, a standard but cosmetic recalculation of the near-surface winds was removed, as noted in text. Horizontal diffusion option is turned off. The land-use database is derived from MODIS.

can capture other aspects of terrain-induced flow (e.g., Jackson et al. 2013; Reinecke and Durran 2009b) as well.

Even with adequate resolution, nearly all model configurations were found to consistently overpredict the winds at most stations in the SDG&E network, despite the adjustments for the nonstandard anemometer height (6.1 m AGL) that were made. Although it could be anticipated that the boundary layer was an important contributor (e.g., Smith 2007), this result was driven largely by the land surface model (LSM). Even the PX–ACM2 configuration had some issues, including possessing larger MAEs for windier stations, and the tendency to simultaneously overpredict less windy sites and underpredict flow speeds in windier areas of the network. In other words, the bias itself was biased. Other physics combinations, including the popular Noah–YSU configuration, resulted in a similar wind speed-dependent bias, just superposed on a larger, positive network-average mean error.

We infer from these results that event-averaged station bias represents the convolution of correctable and inherent errors, and that the PX–ACM2 combination has minimized the former relative to other configurations. In the next part of this study, we pursue the idea

that the inherent error represents very small-scale influences that cannot possibly be resolved, even on a 667-m grid, features that permit the wind to vary over such small scales as previously discussed in the context of Fig. 5b. Part II will also explain why some LSMs outperformed others with respect to wind forecast skill.

It remains, however, that the PX–ACM2 simulation did a reasonable job of capturing the evolution and characteristics of this event. The model was then used to fill in gaps in the observations, especially the vertical structure of the wind field. Vertical cross sections revealed that the aforementioned jumplike feature did form on the west-facing slope, and did appear to be a hydraulic jump with reversed (upslope) near-surface flow. As observed, the simulated jump subsequently progressed upslope during the conclusion of the first phase of the event. The model also showed that while the winds were observed to be weak across the network during the afternoon lull, they actually stayed relatively strong near the ridgeline, in an area largely devoid of stations. Also captured by the model was the more uniform downslope flow that occurred during the event's second phase. These variations are of interest to local meteorologists as they help them understand what kinds of winds can occur at various places and times.

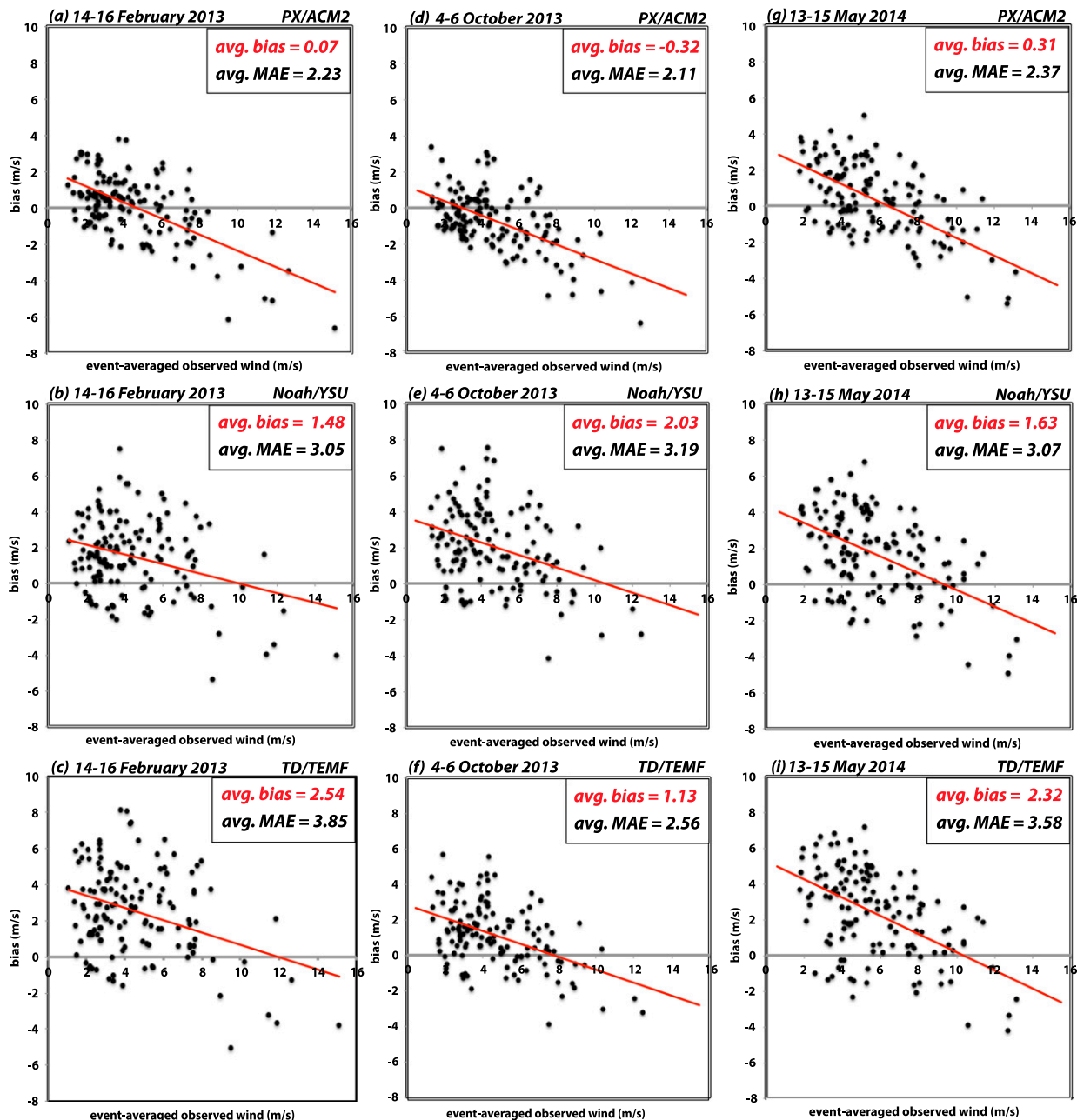


FIG. 18. Scatterplots of event-mean observed wind vs bias for SDG&E stations for three different Santa Ana wind events (columns), and three different LSM/PBL configurations (rows). A least squares fit (red line) is shown on each figure for reference. A version of (a) also appeared in Fig. 10.

Clearly, other variables such as temperature and humidity are also important for fire weather, and our experience has been that the Noah-based schemes, including Noah-MP (Niu et al. 2011), generally emerge as better with respect to MAE and bias (not shown). This motivates us to further investigate the difference among LSMs in predicting winds. Accordingly, the next part of this study will examine how and why model physics influences

forecast skill with respect to the sustained winds, what needs to be done to the Noah-based schemes to improve their wind forecast skill, and will address the important issue of gust parameterization, as the greatest concern is the impact of these high-frequency, small-scale wind bursts that models of the present time cannot resolve. As in the present study, a key role will be played by the exceptionally dense and homogeneous SDG&E network.

Acknowledgments. This research was sponsored by the San Diego Gas and Electric Company. The authors thank Steve Vanderburg and Brian D'Agostino of San Diego Gas and Electric for their assistance and support. Travis Wilson designed many scripts involved in the verification, which employed the Model Evaluation Tools (MET) package from the Developmental Testbed Center. The authors would also like to acknowledge high-performance computing support from Yellowstone (ark:/85065/d7wd3xhc) provided by NCAR's Computational and Information Systems Laboratory, sponsored by the National Science Foundation. The authors thank the three anonymous reviewers for their constructive suggestions.

REFERENCES

- Angevine, W. M., H. Jiang, and T. Mauritsen, 2010: Performance of an eddy diffusivity-mass flux scheme for shallow cumulus boundary layers. *Mon. Wea. Rev.*, **138**, 2895–2912, doi:10.1175/2010MWR3142.1.
- Brinkmann, W. A. R., 1974: Strong downslope winds at Boulder, Colorado. *Mon. Wea. Rev.*, **102**, 592–602, doi:10.1175/1520-0493(1974)102<0592:SDWABC>2.0.CO;2.
- Cao, Y., 2015: The Santa Ana Winds of Southern California in the context of fire weather. Ph.D. thesis, University of California, Los Angeles, 173 pp.
- Chang, C.-H., and F. P. Schoenberg, 2011: Testing separability in marked multidimensional point processes with covariates. *Ann. Inst. Stat. Math.*, **63**, 1103–1122, doi:10.1007/s10463-010-0284-7.
- Chanson, H., 2009: Current knowledge in hydraulic jumps and related phenomena. A survey of experimental results. *Eur. J. Mech.*, **28B**, 191–210, doi:10.1016/j.euromechflu.2008.06.004.
- Chen, F., and J. Dudhia, 2001: Coupling an advanced land surface-hydrology model with the Penn State–NCAR MM5 modeling system. Part I: Model implementation and sensitivity. *Mon. Wea. Rev.*, **129**, 569–585, doi:10.1175/1520-0493(2001)129<0569:CAALSH>2.0.CO;2.
- Doyle, J. D., and D. R. Durran, 2004: Recent developments in the theory of atmospheric rotors. *Bull. Amer. Meteor. Soc.*, **85**, 337–342, doi:10.1175/BAMS-85-3-337.
- Durran, D. R., 1986: Another look at downslope windstorms. Part I: The development of analogs to supercritical flow in an infinitely deep, continuously stratified fluid. *J. Atmos. Sci.*, **43**, 2527–2527, doi:10.1175/1520-0469(1986)043<2527:ALADWP>2.0.CO;2.
- , 1990: Mountain waves and downslope winds. *Atmospheric Processes over Complex Terrain*, Meteor. Monogr., No. 45, Amer. Meteor. Soc., 59–81.
- , 2003: Downslope winds. *Encyclopedia of Atmospheric Sciences*, G. North, J. Pyle, and F. Zhang, Eds., Elsevier Science, 644–650.
- , and J. B. Klemp, 1987: Another look at downslope winds. Part II: Nonlinear amplification beneath wave-overturning layers. *J. Atmos. Sci.*, **44**, 3402–3412, doi:10.1175/1520-0469(1987)044<3402:ALADWP>2.0.CO;2.
- Ek, M. B., K. E. Mitchell, Y. Lin, E. Rogers, P. Grunmann, V. Koren, G. Gayno, and J. D. Tarpley, 2003: Implementation of Noah land surface model advances in the National Centers for Environmental Prediction operational mesoscale Eta model. *J. Geophys. Res.*, **108**, 8851, doi:10.1029/2002JD003296.
- Hong, S.-Y., Y. Noh, and J. Dudhia, 2006: A new vertical diffusion package with an explicit treatment of entrainment processes. *Mon. Wea. Rev.*, **134**, 2318–2341, doi:10.1175/MWR3199.1.
- Huang, C., Y. L. Lin, M. L. Kaplan, and J. J. Charney, 2009: Synoptic-scale and mesoscale environments conducive to forest fires during the October 2003 extreme fire event in Southern California. *J. Appl. Meteor. Climatol.*, **48**, 553–579, doi:10.1175/2008JAMC1818.1.
- Hughes, M., and A. Hall, 2010: Local and synoptic mechanisms causing Southern California's Santa Ana winds. *Climate Dyn.*, **34**, 847–857, doi:10.1007/s00382-009-0650-4.
- Iacono, M. J., J. S. Delamere, E. J. Mlawer, M. W. Shephard, S. A. Clough, and W. D. Collins, 2008: Radiative forcing by long-lived greenhouse gases: Calculations with the AER radiative transfer models. *J. Geophys. Res.*, **113**, D13103, doi:10.1029/2008JD009944.
- Jackson, P. L., G. Mayr, and S. Vosper, 2013: Dynamically-driven winds. *Mountain Weather Research and Forecasting*, F. K. Chow, S. F. J. D. Wekker, and B. J. Snyder, Eds., Springer-Verlag, 121–218.
- Janjić, Z. I., 1994: The step-mountain Eta coordinate model: Further developments of the convection, viscous sublayer, and turbulence closure schemes. *Mon. Wea. Rev.*, **122**, 927–945, doi:10.1175/1520-0493(1994)122<0927:TSMECM>2.0.CO;2.
- Jones, C., F. Fujioka, and L. M. V. Carvalho, 2010: Forecast skill of synoptic conditions associated with Santa Ana winds in Southern California. *Mon. Wea. Rev.*, **138**, 4528–4541, doi:10.1175/2010MWR3406.1.
- Klemp, J. B., and D. R. Lilly, 1975: The dynamics of wave-induced downslope winds. *J. Atmos. Sci.*, **32**, 320–339, doi:10.1175/1520-0469(1975)032<0320:TADOWID>2.0.CO;2.
- Mass, C. F., D. Ovens, K. Westrick, and B. A. Colle, 2002: Does increasing horizontal resolution produce more skillful forecasts? *Bull. Amer. Meteor. Soc.*, **83**, 407–430, doi:10.1175/1520-0477(2002)083<0407:DIHRPM>2.3.CO;2.
- National Wildfire Coordinating Group, 2014: Interagency Wildland Fire Weather Station Standards and Guidelines (PMS 426-3). National Wildfire Coordinating Group, 52 pp. [Available online at <http://www.nwccg.gov/publications/interagency-wildland-fire-weather-station-standards-and-guidelines>.]
- Niu, G.-Y., and Coauthors, 2011: The community Noah land surface model with multiparameterization options (Noah-MP): 1. Model description and evaluation with local-scale measurements. *J. Geophys. Res.*, **116**, D12109, doi:10.1029/2010JD015139.
- NOAA, 1998: Automated Surface Observing System (ASOS) user's guide. National Oceanic and Atmospheric Administration, 72 pp. [Available online at <http://www.nws.noaa.gov/asos/pdfs/aum-toc.pdf>.]
- Oke, T. R., 1987: *Boundary Layer Climates*. Routledge, 435 pp.
- Peltier, W. R., and T. L. Clark, 1979: The evolution and stability of finite-amplitude mountain waves. Part II: Surface wave drag and severe downslope windstorms. *J. Atmos. Sci.*, **36**, 1498–1529, doi:10.1175/1520-0469(1979)036<1498:TEASOF>2.0.CO;2.
- Pleim, J. E., 2007a: A combined local and nonlocal closure model for the atmospheric boundary layer. Part I: Model description and testing. *J. Appl. Meteor. Climatol.*, **46**, 1383–1395, doi:10.1175/JAM2539.1.
- , 2007b: A combined local and nonlocal closure model for the atmospheric boundary layer. Part II: Application and evaluation in a mesoscale meteorological model. *J. Appl. Meteor. Climatol.*, **46**, 1396–1409, doi:10.1175/JAM2534.1.

- , and A. Xiu, 1995: Development and testing of a surface flux and planetary boundary layer model for application in meso-scale models. *J. Appl. Meteor.*, **34**, 16–32, doi:10.1175/1520-0450-34.1.16.
- Raphael, M., 2003: The Santa Ana winds of California. *Earth Interact.*, **7**, doi:10.1175/1087-3562(2003)007<0001:TSAWOC>2.0.CO;2.
- Reinecke, P. A., and D. R. Durran, 2009a: Initial-condition sensitivities and the predictability of downslope winds. *J. Atmos. Sci.*, **66**, 3401–3418, doi:10.1175/2009JAS3023.1.
- , and —, 2009b: The overamplification of gravity waves in numerical solutions to flow over topography. *Mon. Wea. Rev.*, **137**, 1533–1549, doi:10.1175/2008MWR2630.1.
- Schamp, H., 1964: *Die Winde der Erde und ihre Namen (The Winds of the Earth and Their Names)*. Franz Steiner Verlag, 94 pp.
- Sheridan, P. F., and S. B. Vosper, 2006: A flow regime diagram for forecasting lee waves, rotors and downslope winds. *Meteor. Appl.*, **13**, 179–195, doi:10.1017/S1350482706002088.
- Shin, H. H., S. Y. Hong, and J. Dudhia, 2012: Impacts of the lowest model level height on the performance of planetary boundary layer parameterizations. *Mon. Wea. Rev.*, **140**, 664–682, doi:10.1175/MWR-D-11-00027.1.
- Skamarock, W. C., and Coauthors, 2008: A description of the Advanced Research WRF version 3. Tech. Note NCAR/TN-475+STR, 113 pp., doi:10.5065/D68S4MVH.
- Small, I. J., 1995: Santa Ana winds and the fire outbreak of fall 1993. NOAA Tech. Memo., National Oceanic and Atmospheric Administration, National Weather Service Scientific Services Division, Western Region, 30 pp. [NTIS PB-199520.]
- Smith, R. B., 2007: Interacting mountain waves and boundary layers. *J. Atmos. Sci.*, **64**, 594–607, doi:10.1175/JAS3836.1.
- , J. D. Doyle, Q. Jiang, and S. A. Smith, 2007: Alpine gravity waves: Lessons from MAP regarding mountain wave generation and breaking. *Quart. J. Roy. Meteor. Soc.*, **133**, 917–936, doi:10.1002/qj.103.
- Sommers, W. T., 1978: LFM forecast variables related to Santa Ana wind occurrences. *Mon. Wea. Rev.*, **106**, 1307–1316, doi:10.1175/1520-0493(1978)106<1307:LFVRTS>2.0.CO;2.
- Stensrud, D. J., 2007: *Parameterization Schemes: Keys to Understanding Numerical Weather Prediction Models*. Cambridge University Press, 488 pp.
- Sukoriansky, S., B. Galperin, and V. Perov, 2006: A quasi-normal scale elimination model of turbulence and its application to stably stratified flows. *Nonlinear Processes Geophys.*, **13**, 9–22, doi:10.5194/npg-13-9-2006.
- Tyner, B., A. Aiyyer, J. Blaes, and D. R. Hawkins, 2015: An examination of wind decay, sustained wind speed forecasts, and gust factors for recent tropical cyclones in the mid-Atlantic region of the United States. *Wea. Forecasting*, **30**, 153–176, doi:10.1175/WAF-D-13-00125.1.
- Verkaik, J. W., 2000: Evaluation of two gustiness models for exposure correction calculations. *J. Appl. Meteor.*, **39**, 1613–1626, doi:10.1175/1520-0450(2000)039<1613:EOTGMF>2.0.CO;2.
- Vosper, S. B., 2004: Inversion effects on mountain lee waves. *Quart. J. Roy. Meteor. Soc.*, **130**, 1723–1748, doi:10.1256/qj.03.63.
- Wei, H., M. Segal, W. J. Gutowski, Z. Pan, R. W. Arritt, and J. W. A. Gallus, 2001: Sensitivity of simulated regional surface thermal fluxes during warm advection snowmelt to selection of the lowest model level height. *J. Hydrometeorol.*, **2**, 395–406, doi:10.1175/1525-7541(2001)002(0395:SOSRST)2.0.CO;2.
- Westerling, A. L., D. R. Cayan, T. J. Brown, B. L. Hall, and L. G. Riddle, 2004: Climate, Santa Ana winds and autumn wildfires in Southern California. *Eos, Trans. Amer. Geophys. Union*, **85**, 289–296, doi:10.1029/2004EO310001.
- Wieringa, J., 1976: An objective exposure correction method for average wind speeds measured at a sheltered location. *Quart. J. Roy. Meteor. Soc.*, **102**, 241–253, doi:10.1002/qj.49710243119.
- WMO, 2010: Guide to Meteorological Instruments and Methods of Observation. WMO Rep. 8, Secretariat of the WMO (World Meteorological Organization), Geneva, Switzerland, 716 pp.
- Xiu, A., and J. E. Pleim, 2001: Development of a land surface model. Part I: Application in a mesoscale meteorological model. *J. Appl. Meteor.*, **40**, 192–209, doi:10.1175/1520-0450(2001)040<0192:DOALSM>2.0.CO;2.
- Yoshino, M. M., 1975: *Climate in a Small Area: An Introduction to Local Meteorology*. University of Tokyo Press, 549 pp.
- Zängl, Z., A. Gohm, and F. Obleitner, 2008: The impact of the PBL scheme and the vertical distribution of model layers on simulations of Alpine foehn. *Meteor. Atmos. Phys.*, **99**, 105–128, doi:10.1007/s00703-007-0276-1.